A re-analysis of the Jovian radio emission as seen by Cassini-RADAR and evidence for time variability

Moeckel, C.; Janssen, M.; de Pater, I.

DOI
10.1016/j.icarus.2018.12.013

Publication date
2019

Document Version
Final published version

Published in
Icarus

Icarus 321 (2019) 994–1012

Contents lists available at ScienceDirect

Icarus

journal homepage: www.elsevier.com/locate/icarus

A re-analysis of the Jovian radio emission as seen by Cassini-RADAR and evidence for time variability

C. Moeckel[*,a,b,c], M. Janssen[b], I. de Pater[a,c]

[a] Department of Earth and Planetary Science, University of California, McCone Hall, Berkeley, CA 94720, United States
[b] Jet Propulsion Laboratory, California Institute of Technology, Pasadena, CA 91108, United States
[c] Faculty of Aerospace Engineering, Delft University of Technology, HS Delft 2629 The Netherlands

ARTICLE INFO

Keywords:
Jupiter
Magnetosphere
Radio observations

ABSTRACT

After more than a decade of operation at Titan and Saturn, the Cassini RADAR instrument is considered well understood and calibrated. In light of the recent Juno mission which is exploring the inner magnetosphere and the atmosphere of Jupiter, it is worthwhile to reconsider the original measurements of Cassini at Jupiter. The better instrument knowledge in combination with a better understanding of the ammonia distribution of Jupiter has allowed for revising the synchrotron flux density to 1.10 ± 0.07 Jansky, a factor of 2.5 larger than the initial estimate (Bolton et al., 2002). The forward model reduced uncertainties pertaining to the spacecraft pointing using a Markov-Chain Monte Carlo algorithm and constrained simultaneously a brightness model of Jupiter with a disk-averaged brightness temperature of 158.6 ± 2.4 K and depletion of ammonia at the poles (limb darking coefficient, $p = 0.05$). The flux density spectrum for the 2001 measurement campaign reveals a depletion of energetic electrons (>30 MeV) in contrast to an undisturbed electron population at lower energies. Comparing the Cassini radio maps to Very Large Array maps revealed a redistribution of energetic particles to higher latitudes, indicating enhanced pitch angle scattering for energetic particles. This kind of behavior has been observed in the terrestrial Van Allen belts and could be caused by the resonance of energetic electrons with electromagnetic ion cyclotron waves. We used a simplified analytic expression to determine the feasibility of this process at Jupiter. Although this process is not feasible under nominal conditions, a 10-fold enhancement of the cold plasma density, caused for example by extreme UV events, or volcanic eruptions on Io, could lead to rapid pitch angle scattering of electrons, and the subsequent removal of these particles by the atmosphere.

1. Introduction

With the development of the first radio telescopes, a new spectral window was opened into the universe, which led to the accidental discovery of Jupiter's radio emission in the low MHz region (Burke and Franklin, 1955). Since then, Jupiter has been monitored across many different frequencies: In the middle and upper GHz regime (≥5 GHz) the radio waves originate from different depths of the atmosphere, whereas in the lower GHz regime (<5GHz), the non-thermal radiation emitted by high energy electrons dominates the emission. At frequencies below 40 MHz, the radio emissions observed from Earth are characterized by bursts of decametric radiation from coherent cyclotron emission. These radio bursts were the original signal that (Burke and Franklin, 1955) picked up during the first radio scans of the sky.

This paper focuses on the synchrotron radiation, that is the non-thermal radiation from the electrons in the inner magnetosphere (<6 Jupiter radii (R_J)). The synchrotron radiation extends from ~100 MHz regime (Girard et al., 2016) well into the GHz regime (de Pater and Dunn, 2003), with extensive studies in the lower GHz region. The frequency of the synchrotron radiation depends on the energy of the electrons and the local magnetic field strength. In this paper, the term highly energetic electrons refers to particles with energies above 30 MeV, whereas lower energy refers to the particles between 1 MeV and 30 MeV.

At higher frequencies, the thermal emission from Jupiter's atmosphere dominates and a successful retrieval of the synchrotron radiation relies on accounting for the thermal emission, by relying on the polarization of synchrotron radiation (de Pater et al., 1982) and/or spatial separation of the signal, e.g., (de Pater and Dunn, 2003).

As the Juno mission continues its course through the Jovian system (Bolton et al., 2017), the first measurements indicate that the radiation belts are more complex than our current models can capture (Santos-

* Corresponding author at: Department of Earth and Planetary Science, University of California, McCone Hall, Berkeley, CA 94720, United States.
E-mail address: chris.moeckel@berkeley.edu (C. Moeckel).

https://doi.org/10.1016/j.icarus.2018.12.013
Received 10 December 2017; Received in revised form 30 November 2018; Accepted 4 December 2018
Available online 07 December 2018
0019-1035/

Costa et al., 2017). On top of that, spatial variations in the ammonia distribution, a consequence of the differences in local conditions for cloud condensation, are highly suggestive of the complex dynamics in Jupiter's upper troposphere (0.5–3 bars) (de Pater et al., 2016; Li et al., 2017). The Cassini radio measurements are also sensitive to the ammonia variation in Jupiter's troposphere via thermal blackbody radiation, since the receiver operates in the vicinity of the ammonia absorption band.

The time variability of the synchrotron radiation, which has been observed on time scales of years (Klein, 1976), of weeks (Miyoshi et al., 1999; Kita et al., 2013; 2015) and of days (de Pater et al., 1997b) can highlight the various processes that deliver energetic electrons (of order MeV) to the inner magnetosphere, e.g., radial diffusion (Bolton et al., 1989; de Pater and Goertz, 1994) or through shock acceleration (Brecht et al., 2001).

Monitoring the emission at different frequencies allows for probing electrons at different energy levels and different locations in the magnetic field. When done simultaneously, we can infer the energy distribution of the electrons and probe the linkage between the various energy levels. It is generally thought that disturbances can be seen across the frequency spectrum (Carr et al., 1983; de Pater et al., 2003; Bolton et al., 2004).

A first attempt to map the electrons in Jupiter's magnetic field at frequencies above 10 GHz (Janssen et al., 2001; Bolton et al., 2002), was conducted with the 4-m communication antenna at 13.8 GHz onboard the Cassini spacecraft while en-route to Saturn. At these frequencies, the radiation originates from particles at highly relativistic speeds. The measurements indicate a strong depletion of energetic particles; a finding that could not be replicated using synchrotron diffusion models (de Pater and Dunn, 2003; Santos-Costa et al., 2014). Concurrent measurements at lower frequencies with the VLA (Janssen et al., 2001; Santos-Costa et al., 2014) returned synchrotron fluxes within the observed variability. These data, however, indicated that the electrons were differently distributed than previously observed, with a curious enhancement at $R > 1.7\,\mathrm{R_J}$. Nevertheless, these findings do not sufficiently address the question what could have caused the strong depletion of the energetic electrons at higher frequencies.

The early nature of instrument operation, however, also leaves the possibility that instrument artifacts have propagated into the retrieval. To investigate possible effects, we make use of the improved understanding of the instrument's performance and calibration after years of operation in the Saturnian system (Janssen et al., 2009; 2013; 2016). This motivates a new retrieval of the Jovian synchrotron radiation and allows for minimizing and mitigating possible systematic artifacts that affected the initial retrieval. In this paper we aim to (1) re-evaluate the distribution of ultra-relativistic electrons in Jupiter's magnetosphere, (2) constrain the flux density of the synchrotron radiation at 13.8 GHz, (3) reduce the uncertainties of the disk-averaged brightness temperature at the same frequency; and (4) offer a possible mechanism that could explain the Cassini synchrotron measurements.

First, we present a brief overview of the instrument and the dataset, after which we explain the calibration and retrieval process of the instrument and how it was refined compared to the initial retrieval. The results highlight the main finding of the re-calibration, and the discussion aims at explaining the depletion of energetic electrons.

2. Instrument and data

The Cassini RADAR experiment was designed for its primary purpose of studying Titan's surface, by using active and passive modes of operation. The receiver relies on the onboard 4-m communication antenna, in combination with a Cassegrain receiver and a passive radiometer that collects radiation at a frequency of 13.78 GHz; the main characteristics of the instrument are summarized in Table 1 (Elachi et al., 2004).

Cassini passed Jupiter on December, 30th 2000 at a minimum distance of 136 R_J. Observations with the radio receiver were allocated for the 2nd and 3rd of January when the spacecraft was receding from Jupiter, but within 150 R_J. The relative position and orientation of the spacecraft were obtained using the latest Cassini - SPICE kernels (Spacecraft, Planet, Instrument, Camera-matrix, Events), a toolkit that accesses the relevant spacecraft geometry. The instrument is operated by moving its boresight in a raster pattern across the main synchrotron region (8 $R_J \times 6$ R_J centered on Jupiter) as shown in Fig. 1, and is recording the corresponding voltage on the radiometer. The recorded signal is a product of the brightness of the sky and the instrument beam pattern, that describes the spatial sensitivity of the antenna to the incoming radiation. The beam pattern outwards to 2° was established through sun scans prior to Saturn orbit insertion (Janssen et al., 2009). The extended beam pattern as found during the operation on Titan and Saturn is not of concern for this research, as Jupiter remains throughout all the scans within 2°.

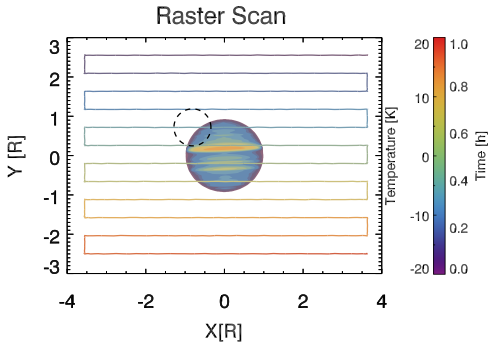

Fig. 1. Raster scan of Jupiter's inner magnetosphere where the colors indicate the duration of the scan. The contours of the planet refer to the temperature above a uniform disk of 158.6 K, where the color scale is given on the right of the colorbar. The pattern on the sky to be scanned is set conservatively to cover the region where the main emission is originating from. The scale of the main beam corresponding to the half power beam width of 0.36° as given in Table 1 is given by the dashed line. (For interpretation of the references to color in this figure legend, the reader is referred to the web version of this article.)

Mapping the total emission with a polarized antenna requires two orthogonal measurements; in case of Cassini, that was achieved by rotating the spacecraft after one Jupiter rotation to obtain the complementary polarization plane. The total observation consists of 20 individual scans, 10 at each polarization, with a single scan duration of one hour. The scans are numbered, where scan 1–10 refer to the vertical polarization measurements, and scan 11–20 indicate the horizontal polarization measurements.

3. Retrieval

Retrieving the synchrotron radiation residuals from the raw measurements required several steps. After calibrating the instrument based on a-priori knowledge, calibration artifacts were removed through the so-called baseline subtraction. The synchrotron radiation is essentially the residual in the data after subtracting Jupiter's thermal radiation from the observations, where the parameters of Jupiter's thermal contribution were obtained through an iterative process. This allowed for

Table 1
Main characteristic of the Cassini RADAR instrument (Elachi et al., 2004).

Instrument		Beam properties	
Frequency	13.78 GHz	Half power beam width	0.36 deg
Wavelength	2.18 cm	Main beam	$0 < \theta < 0.5$ deg
Bandwidth	135 MHz	Near side lobes	$0.5 < \theta < 2$ deg
1-σ Noise	0.13 K	Far side lobes	$2 < \theta < 60$ deg
Polarization	linear		

solving for the synchrotron and the thermal radiation simultaneously.

3.1. Calibration and stability

In theory, repeated observations of two sources with known emission strength are sufficient to calibrate a radiometer, which relates the recorded sky count, N_{sky}, to the antenna temperature, T_A, an equivalent unit for the brightness of the source when observed by the instrument. Operational constraints of Cassini, however, do not allow for this calibration, resulting in the ad-hoc calibration algorithm (Janssen et al., 2001), that estimates the relevant calibration constants, and corrects for their impact throughout the observation, the so-called baseline subtraction. The calibration constant, *cal*, and the gain, *g*, are best-estimates obtained from a decade of operation of the instrument (Janssen et al., 2009; 2013; 2016). The instrument noise, T_{sys} is based on the temperature of the waveguide, and the final antenna temperature estimate includes a correction for the annual gain drift ($g_d = -0.3\%$ per year, where time, *t*, is given in years) due to instrument degradation. Lastly, the calibration constants were obtained from observations of Titan, requiring a small correction, F_{corr} for its atmospheric contribution:

$$T_A = \frac{cal}{g} N_{sky} - T_{sys} \tag{1}$$

$$T_A = T_A(1 + g_d\, t) F_{corr} \tag{2}$$

3.2. Baseline correction

The turn-around points during the raster motion (as seen in Fig. 1) constitutes the furthest distance from Jupiter, and are used to establish the empty sky signal. The empty sky signal is composed of four components: (1) the thermal radiation of Jupiter leaking in through the side lobes; (2) the non-thermal synchrotron radiation picked up through the side lobes; (3) the cosmic microwave background (CMB), and (4) lastly the noise component in the system. The thermal contribution is removed by convolving the beam with an estimate of Jupiter's brightness, which is among the properties that are estimated in this process. This can be solved by using an iterative approach as explained in the methodology. The non-thermal contribution was found to be negligible at the turn-around point, and thus can be neglected. Regarding the CMB, the subtraction process also removes this weak signal, with a physical temperature of 2.7 K and a Rayleigh-Jeans equivalent radio temperature at Cassini's frequency of 2.4 K (Gibson et al., 2005). The final temperature estimates, therefore, have to be corrected for the CMB signal. Lastly, the noise term was canceled by subtracting the empty sky signal from the measurement point. The first order variations in instrument noise are accounted for by interpolating the empty sky signal strength between the turn-around points.

3.3. Residual minimization

The remaining signal after the baseline subtraction is twofold: thermal radiation from the atmosphere and the synchrotron radiation. The basic idea is to model Jupiter's contribution, subtracting it from the received signal and the remaining signal can then be attributed to synchrotron radiation. Since the two signals originate from a different direction in the sky, we used spatial information on separating these two signals. Whereas there is a small contribution of the synchrotron radiation in front of the disk (de Pater and Dunn, 2003, ~5–9%), the majority of the synchrotron radiation originates off the disk. We, therefore, build a three dimensional model of Jupiter's brightness including the zone belt structure (de Pater et al., 2016), with two parameters: the nadir brightness temperature and the limb darkening coefficient in the north-south direction. By convolving the temperature model, T_B, with the beam pattern, *G*, of the Cassini instrument (see Janssen et al. (2009)), the response of the antenna to Jupiter, T_{model}, can be emulated:

$$T_{model} = \frac{\iint_\Omega T_B(\theta, \phi) G(\theta, \phi) d\Omega}{\iint_\Omega G(\theta, \phi) d\Omega} \tag{3}$$

The coordinates, θ and ϕ, are defined in the beam frame so that the brightness model is interpolated in the same frame. This, however, requires accurate knowledge (~10 μrad) of the position of Jupiter, which is more accurate than the pointing requirement of the spacecraft (Pilinski and Lee, 2009). Additional to the pointing uncertainty, there is an indication that the beam pattern is not aligned with boresight of the beam (Zhang et al., 2017) (see Appendix A). These two factors combined result in an offset between Jupiter's real position and the model, introducing large residuals, which can affect the synchrotron radiation retrieval. Whereas the beam offset is invariant, the pointing uncertainty has random and systematic variations. Since there are no independent measurements of the pointing fluctuations, these two effects are combined into a single beam offset, which is kept constant for the duration of a single scan. This is a compromise that allows for sufficient data points to estimate the beam offset, while still being able to track longer-term variations. Lastly, the onboard oscillator is used for time tagging the measurements. The oscillator is drifting over time, resulting in the recorded time lagging behind its true position. This brings the total tally of uncertainties to five that we estimated during the retrieval process.

3.4. Uncertainty reduction

These five uncertainties were reduced through a Markov-Chain Monte-Carlo (MCMC) optimization that correlates the synchrotron residual, with typical synchrotron features. The correlation was based on four regions of interest:

- Far from the planet (>3.5 R_J): the residuals should be purely thermal noise and show no additional structure.
- On the disk (<0.5 R_J): The viewing geometry results in a synchrotron radiation minimum in front of the disk when crossing the Jovian spin axis.
- Limb-crossing (=1R_J): The residual when crossing the limb should be continuous, whereas discontinuities indicate a misalignment of the Jovian brightness model.
- Above the poles (>0.5 R_J): The synchrotron region is concentrated around the equatorial plane, extending up to the secondary emission lobes around 30° latitude. At higher latitudes, no signal is expected.

We developed an algorithm that identified these four regions based on the pointing of the spacecraft and computed a compound cost function based on the strength of the residual at these locations. Fig. 2 visualizes the working principle of the algorithm, where the algorithm identifies and combines the signal at the four regions of interest. The different symbols as explained in the figure legend indicate the locations that are compared.

The signal at these four points is combined in a compound cost function, which correlates the observed signal with a theoretically expected signal, e.g., the minimum when scanning the disk should be close to the spin axis as consequence of the limited path length, or the root mean square of the residual is minimized when far from the planet. The MCMC is then stepping through the solution space while optimizing the cost function, where a small cost function indicates a better agreement. The risk of over-constraining the solution was mitigated by applying different compound cost functions, where the solution was found to converge to a similar solution with minor impact on the final solution. The variations in the solution were included in the uncertainty estimate of the solution. Per individual scan, the MCMC sampled through 3000 different combinations of uncertainties, where the combinations were sampled based on a Gaussian distribution centered

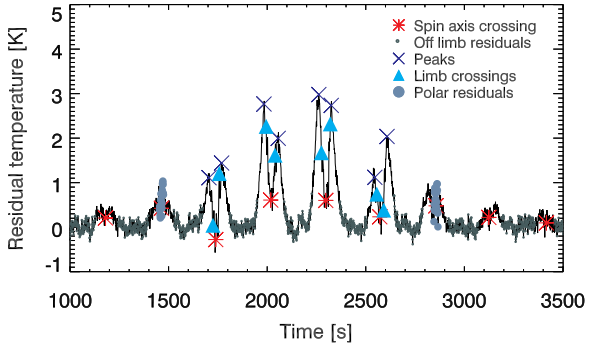

Fig. 2. Residual antenna temperature for Scan 11. The various points are the regions of interest as identified by the algorithm. This is an example of a optimum solution for the given combination of uncertainties: $dt = 0.1$ (s), $dx = 0.39$ (mrad), $dy = 0.57$ (mrad), $T = 162$ (K), $p = 0.05$ and the corresponding value of the cost function is 28.99. The red stars indicate the crossing of the magnetic spin axis and should correspond to a minimum in residuals on the disk. The turquoise triangles indicate the value when crossing the limb and should not coincide with the radiation peaks as identified by the blue crosses. The empty sky residuals shown by the filled dark green circles are minimized, and the grey filled dots identify the residuals originate from above the poles. (For interpretation of the references to color in this figure legend, the reader is referred to the web version of this article.)

around the lowest cost function evaluation. The transition probability of the MCMC is determined by the cost function magnitude. This procedure allowed for finding a combination of uncertainty for each scan, which was used for constructing the radio maps.

4. Results

The results of the Cassini campaign are split into two categories. The constrained uncertainties pertaining to the synchrotron radiation can be found in the first part of the result section, whereas information on the thermal radiation from Jupiter is presented in the second section.

4.1. Uncertainties

As presented in Section 3, each scan has five associated uncertainties, where the final result is derived from a unique combination of these uncertainties. The scan-averaged results for the best-fit uncertainties are summarized in Table 2. The solution is dependent on the orientation of the spacecraft and is therefore presented separately. The behavior of the instrument is further discussed in Appendix A. The characteristics of the thermal contribution of Jupiter converge for both sets of measurements, resulting in robust estimates for the final quantities.

Before presenting the results, it is important to highlight how the uncertainties were derived. Each scan has a unique combination of uncertainty parameters that makes the final results sensitive to the sampling of the MCMC-algorithm and the chosen weights for cost functions. In order to mitigate this effect, the uncertainties are based on the robustness of the solution. The spread in the solution for each MCMC run is reflected in the uncertainties. Small uncertainties are, therefore, an indication that the final result is not sensitive to the chosen parameters. A detailed sensitivity analysis indicated that the beam offset has a minor impact on the result, whereas the chosen parameters for the thermal brightness model have a major impact on the retrieved synchrotron results, with the retrieved flux density having a sensitivity of ~0.1 Jy/K. This sensitivity to the thermal radiation is unique to the Cassini measurements and is a consequence of the extended beam. When the main beam is centered on the synchrotron emission peak, the thermal signal leaking in through the extended sidelobes dwarfs the synchrotron signal by a factor of 10.

The final uncertainties are a combination of various factors that affect the results: (1) variations in the MCMC results, (2) the radiometer noise (Janssen et al., 2009), (3) uncertainty in the calibration scale factor; and (4) the 1% absolute uncertainty of the Cassini radiometer (Janssen et al., 2009). The magnitudes of the uncertainties (in Jansky) are tabulated in Table 3.

Table 2
Averaged parameters for the 10 scans per polarization, where the two orientations of the spacecraft are indicated by vertical and horizontal. The rows are as follows: (1) oscillator drift, (2) beam x-offset from boresight in the spacecraft frame, (3) beam y-offset, (4) the nadir brightness temperature as used in the limb darkened model, and (5) the limb darkening coefficient, p, on the north-south axis in form of $(T(\theta) = T(0)cos(\theta)^p)$. The last two rows indicated the average over all 20 scans.

Parameters	Magnitude	
Polarization	Vertical	Horizontal
dt [s]	0.26	0.17
dx [mrad]	0.33	0.40
dy [mrad]	0.25	0.58
T [K]	161.3	161.8
p [-]	0.05	0.05
Scan averaged		
T [K]	161.5	
p [K]	0.05	

4.2. Radio maps

The residuals, and the boresight pointing information can be combined to map the signal onto the Jupiter system. The 20 radio maps, each map corresponding to an hour long scan, were corrected for the inclination of the magnetic pole (9.5°) [Cf. Appendix B]. The total synchrotron radiation maps shown in Fig. 3 were obtained by combining the individual maps, where the resolution is limited by the beam size of the RADAR instrument (see Table 1). The synchrotron radiation is centered on the equatorial region and has a total extent of 6 R_J (in the equatorial plane) and 4 R_J (out of the plane). The synchrotron radiation peaks in the equatorial surface at 1.47 R_J where the majority of the electrons are gyrating in strong magnetic fields. The inner boundary is determined by the atmospheric loss cone, where particles are lost due to collision with atmospheric particles. Radio maps are generally characterized by three emission rings, the main emission ring centered on the equatorial surface and two secondary emission rings at 30° latitude (de Pater and Sault, 1998). The resolution is too low to distinguish the secondary emission rings, which are attributed to a secondary population that bounces between the mirror points at mid latitude. Their presence, however, cause the north-south elongation in the vicinity of the limb. There is a small equatorial signal in front of the disk, radiated by the electrons in front of Jupiter. The superposition of the strong thermal radiation in combination with the weak synchrotron signal in front of the disk, however, reduces the reliability of the data. Despite including the limb darkening coefficient in the MCMC to account for the radiation in the polar region, there remained a small but discernible signal above the poles. This is surprising as the field lines at these latitudes correspond to large L-shells, including open field lines, which are nominally not populated by energetic electrons.

Lastly, the lack of negative residuals on the disk of Jupiter is a good

Table 3
Cassini's total uncertainty estimate in Jansky.

Radiometer	Calibration	Cal. scale factor	MCMC variations	RMS	Worst case
0.020	0.00	0.013	0.033	0.041	0.074

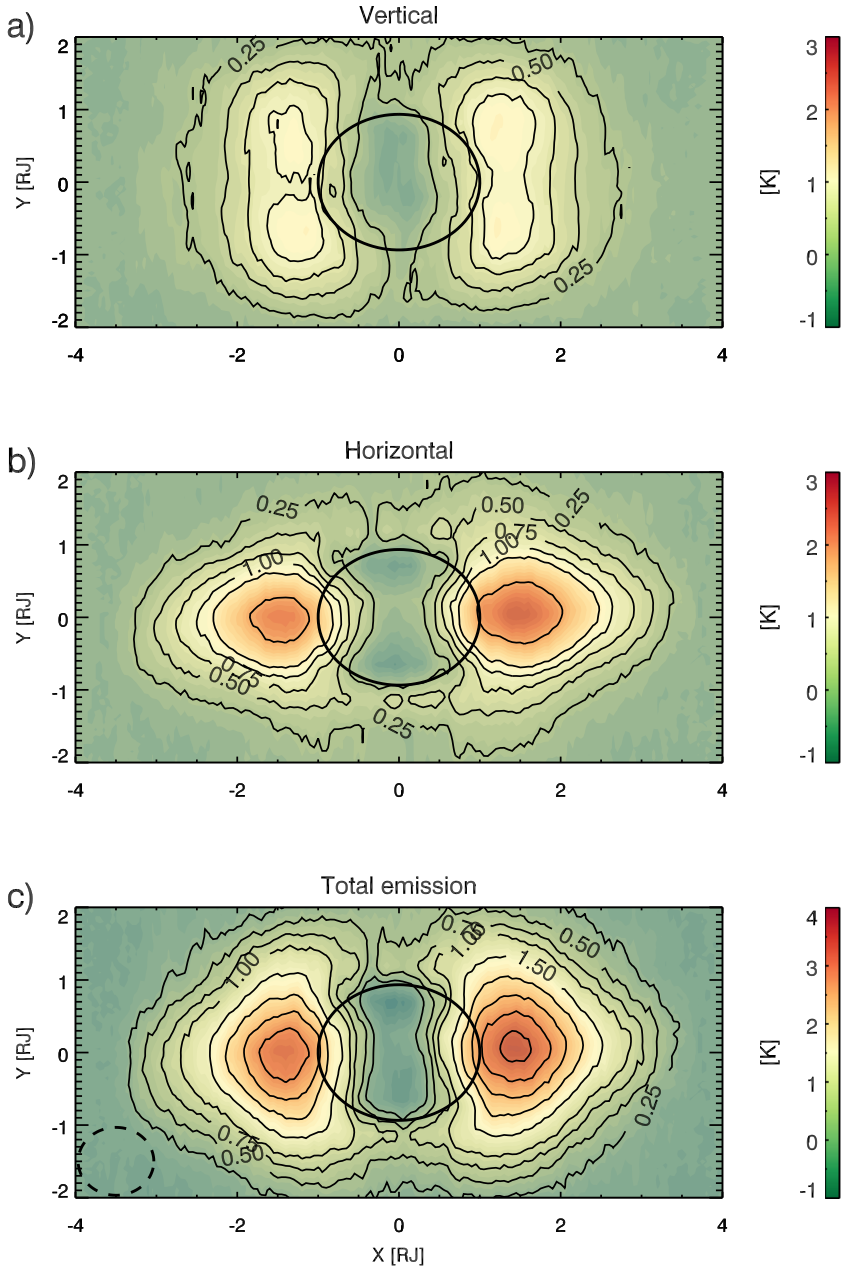

Fig. 3. Synchrotron radiation maps in units of brightness temperature obtained by rotationally averaging the 20 maps and correcting for the magnetic field wobble. The circle in the center indicates the surface of Jupiter, as given by the 1bar pressure level and the dotted line indicates the dimension of the beam size. Panel (a) shows the radio maps of the vertical polarization, panel (b) the horizontal polarization and panel (c) the combined signal. The maximum emission can be found at 1.47 R_J (left) and 1.46 R_J (right); the elongation in the north-south direction is due to the presence of the secondary emission rings.

indication that the brightness model accurately reflects the thermal radiation from Jupiter.

The locations of the emission maxima are tabulated in Table 4, where the high latitude maxima were derived from the vertically polarized maps as seen in panel (a) of Fig. 3. The results agree with locations found at other frequencies (de Pater and Jaffe, 1984; de Pater, 1991).

4.3. Beaming curve

The tilt of the magnetic axis compared to the spin axis causes a modulation of the synchrotron intensity as the planet rotates. Fig. 4 shows this modulation of the intensities with longitude, which were

Table 4
Emission maxima characteristics.

Region	High latitude emission		
	T_B (K)	Distance (R_J)	Latitude (°)
Left upper	2.45	1.44	24
Left lower	2.14	1.45	33
Right upper	2.30	1.44	34
Right lower	2.41	1.37	27
	Equatorial		
Left	3.32	1.47	0
Right	3.64	1.46	0

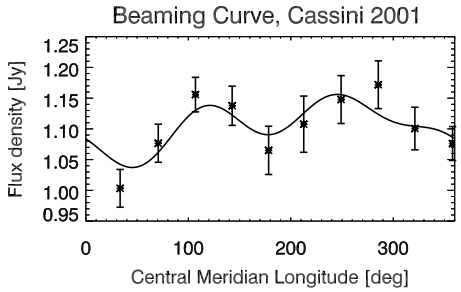

Fig. 4. The variability of the solution obtained from the range of MCMC solutions. The solid lines gives the beaming curve obtained from fitting the measurements to the first three terms of the Fourier expansion.

obtained by combining the vertical and horizontal polarization at corresponding longitudes. The sinusoidal variations are caused by the magnetic wobble of Jupiter's magnetic field, which changes the magnetic declination, D_{mag}, of the observer and as such the viewing geometry. Due to the highly beamed nature of the synchrotron signal, an increase in the magnetic declination causes a reduction in received flux density, resulting in the so-called beaming curve. It is common practice (Klein et al., 1989) to describe the beaming curve, $S(\lambda)$, as a function of the longitude, λ, by a sum of Fourier terms (A_i, ϕ_i):

$$S = A_0\left(1 + \sum_{1}^{3} A_i \sin[i(\lambda + \phi_i)]\right) \quad (4)$$

The best-fit Fourier coefficients to our Cassini data are compared with values obtained with observations spanning many years and for a range of Earth's jovicentric declinations, D_E. The values obtained for Cassini measurements are tabulated in Table 5, with the corresponding uncertainties represented by the error bars in Fig. 4.

4.4. Time variability of the flux density

The integrated flux density scaled to 4.04 AU is known to fluctuate over time (Klein et al., 1989; Miyoshi et al., 1999; Santos-Costa et al., 2008). The low flux density derived from the initial measurements could not be reconciled with synchrotron radiation models nor with comparable measurements at high frequencies (de Pater and Dunn, 2003; Kloosterman et al., 2008). The beaming curve as presented above was used to derive the rotation averaged flux density of 1.10 ± 0.072 Jy for the Cassini measurements. This value is a factor of 2.5 greater than the initial retrieval and confirms that the original retrieval suffered from systematic artifacts. The main reason for the increased flux density is the improved knowledge of the beam pattern (see Janssen et al. (2001) vs Janssen et al. (2009)), enabled by sun scans prior to orbit insertion at Saturn. Due to the limited knowledge of the unexpected large sidelobe at the time, thermal radiation was leaking in through sidelobes that systematically suppressed the synchrotron radiation.

The flux density spectrum details the synchrotron flux across the relevant frequency spectrum and gives information on the energy distribution of the electrons. Fig. 5 shows three different flux density spectra for three measurement campaigns (reference can be found in the caption), highlighting the temporal variations at the low and high frequencies. The 2001 measurements, obtained simultaneously with the Cassini data, are based on the processed maps as presented in Santos-Costa et al. (2014). The values presented in this paper are based on the retrieved maps, which were provided by Daniel Santos-Costa and reprocessed by us using the same methodology applied to the Cassini maps. Each frequency contained four maps averaged over four longitude bands. Due to the lack of longitudinal resolution, the Fourier-series coefficients from the multi-year analysis (Klein et al., 1989) were used to model the higher order sinusoids. Therefore, the four maps were used to constrain the averaged flux density, A_0.

Table 5
Beaming curve obtained from the Cassini measurements, and compared to coefficients (see Table 5 and Eq. (4)) derived from a multi-year analysis for the corresponding declination of − 1. 5° (Klein et al., 1989).

Coefficients	A_0 (Jy)	A_1 (Jy)	ϕ_1 (°)	A_2 (Jy)	ϕ_2 (°)	A_3 (Jy)	ϕ_3 (°)
Cassini radar	1.10	0.031	226.2	0.047	−65.0	0.02	33.9
Multi year analysis	–	0.032	227.3	0.052	−71.3	0.01	−5

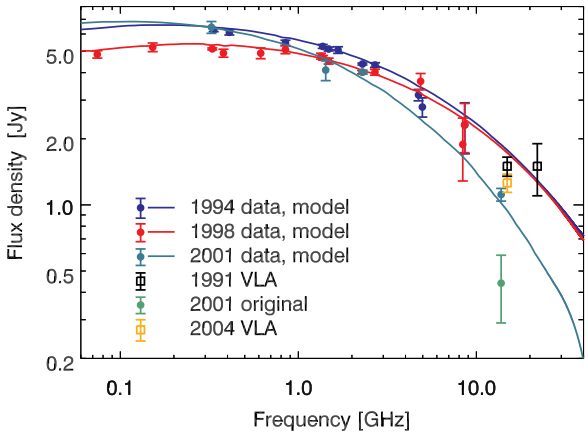

Fig. 5. Flux density spectrum for three observation campaigns. The 1994 (blue) and 1998 (red) observation are obtained from de Pater et al. (2003), the 1991 (black) data points are obtained from de Pater and Dunn (2003) and the 2004 (orange) measurements are presented in Kloosterman et al. (2008). The teal points are obtained from the radio maps presented in Janssen et al. (2001), Bolton et al. (2002) and Santos-Costa et al. (2014) and include the flux density derived from the re-calibration at 13.8 GHz; the fit to the 2001 data points is given by a model calculation for a depleted magnetosphere (de Pater and Dunn, 2003) (c.f. Model dot-dash). The original measurement point from Cassini/RADAR is shown in green. (For interpretation of the references to color in this figure legend, the reader is referred to the web version of this article.)

Based on these measurements, the flux density spectrum can be established and is compared to other measurement campaigns in Fig. 5. The blue and red lines correspond to measurements from 1994 and 1998, to which a synchrotron model was fit (de Pater et al., 2003). These measurements are the result of a worldwide campaign, which involved observations at many different frequencies. The synchrotron model was then fit to the observations to obtain information on the electron population, most notably their energy distribution. Whereas there are plenty of observations at lower frequencies, at higher frequencies, the increased thermal contribution complicates the reliable retrieval of synchrotron flux density. Nevertheless, several authors have managed to retrieve the synchrotron radiation from Very Large Array (VLA) observations at high frequencies, either through spatial separation of the two components, and/or using the polarization characteristics of the non-thermal radiation. These observations are indicated by the black dots (VLA maps in 1991 (de Pater and Dunn, 2003)), and the orange dots (VLA maps in 2004 by Kloosterman et al. (2008)). The low flux density in 2001 (13.8 GHz, 1.1 Jy) compared to the measurements of 2004 (14.9 GHz, 1.26 Jy) (Kloosterman et al., 2008) is indicative of a greatly altered magnetosphere, most likely a depletion of electrons. This becomes even more evident when scaling the 14.9 GHz measurement to Cassini's frequency using the green modeling curve, resulting in a flux density of 1.36 Jy.

This hypothesis is supported considering the good agreement between the 2001 observations (green turquoise dots) and the corresponding model (green turquoise line, taken from de Pater and

Dunn (2003)). The modeling curve corresponds to a magnetosphere where the energetic tail of the electrons was removed artificially, resulting in a low flux density at high frequencies (>5 GHz). The agreement of the model with the 2001 observation campaign confirms that the magnetosphere was depleted of energetic particles (>30 MeV), whereas particles with lower energies were undisturbed.

4.5. Time variations in the spatial distribution

Additional information can be obtained by comparing the Cassini synchrotron radiation maps with VLA maps at different frequencies. There are several considerations that have to be kept in mind when comparing maps directly.

4.5.1. Resolution adjustment

First, the size of the beam determines the spatial resolution of the map. The Cassini beam, despite the spacecraft's relatively short distance to the planet, has a large beam size compared to the interferometric VLA beam. As a consequence the high resolution data must be degraded in resolution where we make use of the convolution theorem (Hirschman and Widder, 2012): by convolving the VLA beam (σ_{VLA}) with a synthesis Gaussian (σ_{SYN}) to match the Cassini beam size (σ_{CAS}), so that $\sigma^2_{VLA} + \sigma^2_{SYN} = \sigma^2_{CAS}$. As a consequence, details such as the high latitude emission rings disappear from the radio maps, and the emission region becomes wider and less pronounced.

4.5.2. Normalization

The electron number population follows a power law, resulting in weaker emission at higher frequencies, which can be seen directly in Fig. 5. Comparing maps in absolute units is dominated by the difference in flux density rather than details in the structure. Therefore, the maps are normalized by the peak flux density in the vicinity of the planet (see Table 4). There are some expected behaviors when comparing normalized maps at different frequencies. The frequency of the emission is tied to the energy of the particles, E, and the magnetic field strength, B, $\nu \sim E^2 B$ (Ginzburg and Syrovatskii, 1965). The further away from the planet, the less acceleration the particles have undergone, resulting in a low energy electron population. In combination with lower magnetic field strength the synchrotron radiation will peak at lower frequencies according to the above equation. The normalized maps at lower frequencies are therefore expected to dominate the regions far from the planet. In contrast, at higher latitudes, the increase in the magnetic field strength causes a stronger emission at higher frequencies.

4.5.3. Rotational-averaging

The Cassini maps are produced for two complete rotations of the planet. Often the VLA maps only have limited observation time, and capturing a complete rotation is not always possible (Kloosterman et al., 2008). Higher order moments in the magnetic field in combination with the magnetic latitude of the observation can alter the structure of the radio maps and thus affect the averaging result. Nevertheless, these effects are often on smaller scales, and the resolution degradation mitigates this to a degree. Similarly, the viewing geometry as determined by Earth declination (D_E) (Dulk et al., 1997; 1999); these variations, however, were found to be small (Kloosterman et al., 2005). The adjustments as detailed above, however, will reduce the impact of these factors.

The following paragraphs compare the normalized Cassini maps (13.8 GHz, $D_E = -1.5°$) to observations at high frequencies (Fig. 6a), 14.9 GHz, $D_E = -1.72°$ (Kloosterman et al., 2008)) and at lower frequencies (Fig. 6b), 1.4 GHz, $D_E = 3.44°$) and (Fig. 6c), 1.4 GHz, $D_E = 3.58°$) (Santos-Costa et al., 2014).

4.5.4. Comparison with the Ku-band (14.9 GHz)

The high-frequency maps at the Ku-band probe the most energetic particles in the Jovian magnetosphere. At these frequencies, the receiver is sensitive to electrons with kinetic energies of ≈40–50 MeV (for a magnetic field strength, B, ≈1.5 Gauss at 1.5 R_J).

Fig. 6(a) visualizes the normalized difference between the Cassini maps and VLA maps, where red refers to an enhancement of the Cassini measurements, and blue indicates a stronger signal from the VLA maps. The enhancement of the Cassini maps at high latitudes is concentrated around the latitudes of the secondary emission rings, and therefore supports the conclusion of Santos-Costa et al. (2014) that at the time of the flyby the Jovian magnetosphere was profoundly disturbed. Furthermore, the high latitude rings are produced by pitch angle scattering inwards of Amalthea (de Pater et al., 1997a) and as such indicates increased scattering activity inside the orbit of Amalthea. Note, that the signal in front of the disk should not be trusted as the zone-belt structure was ignored in the original analysis (Kloosterman et al., 2008). Lastly, the comparison highlights the enhancement above the poles, indicating the disturbance in the magnetosphere was not localized but affected the complete synchrotron radiation region.

4.5.5. Comparison with the L-band

It must be cautioned that the low flux density of 3.79 Jy recorded in 1988 (Santos-Costa et al., 2014) (compared to 5.2 Jy and 4.6 Jy as measured in 1994 and 1998 by de Pater et al. (2003)) implies that radiation belts were depleted in electrons for electrons around 15 MeV (corresponding to a distance of 1.5 R_J). The comparison between the normalized L-band measurements of 1988 in Fig. 6(c) and 2001 in Fig. 6(b) (Santos-Costa et al., 2014), nevertheless, is very insightful. The main detail that comes to attention in the 1988 maps is the strong enhancement of the secondary emission rings, indicating that energetic electrons must have been pitch angle scattered to higher latitudes. The equatorial regions compare relatively well in the normalized maps for both epochs. The low frequency maps, probing less energetic particles further away from the planet, should show a depletion at greater distances from the planet in the comparative maps. In the 2001 maps, this systematic effect can be seen, where the depletion at distances greater than 2 R_J can be clearly distinguished. The comparison with the 1988 maps, however, shows that even at location of Amalthea (2.5 R_J) the high frequency maps are still enhanced, indicating that the energetic electrons must have been more spatially distributed. The L-shells at which the enhancement can be found, corresponds to the equatorial region around Amalthea, supporting the hyopthesis that Amalthea pitch-angle scattered electrons. Both observations require processes that must have accelerated particles to sufficient energies as far outwards as Amalthea and at the same time redistributed these particles to cause the enhancement at higher latitudes. A possible explanation is presented in Section 5.

4.6. Thermal radiation

The MCMC was set up to include two parameters of the thermal brightness model of Jupiter: the brightness temperature, and polar limb-darkening coefficient. The east-west limb darkening was hard to constrain due to the poor resolution of the Cassini RADAR beam and thus obtained from de Pater et al. (2016). The reliability of the solution can be tested by an analysis of the residuals on the disk of Jupiter. The overall residuals are centered around 0 with a standard deviation that is similar to the noise in the instrument, indicating no remaining structure. When integrating the thermal brightness and averaging over the disk, we obtain a disk-averaged brightness temperature of 158.6 ± 2.4 K, after correcting for the CMB. This value is within the 1 σ of the

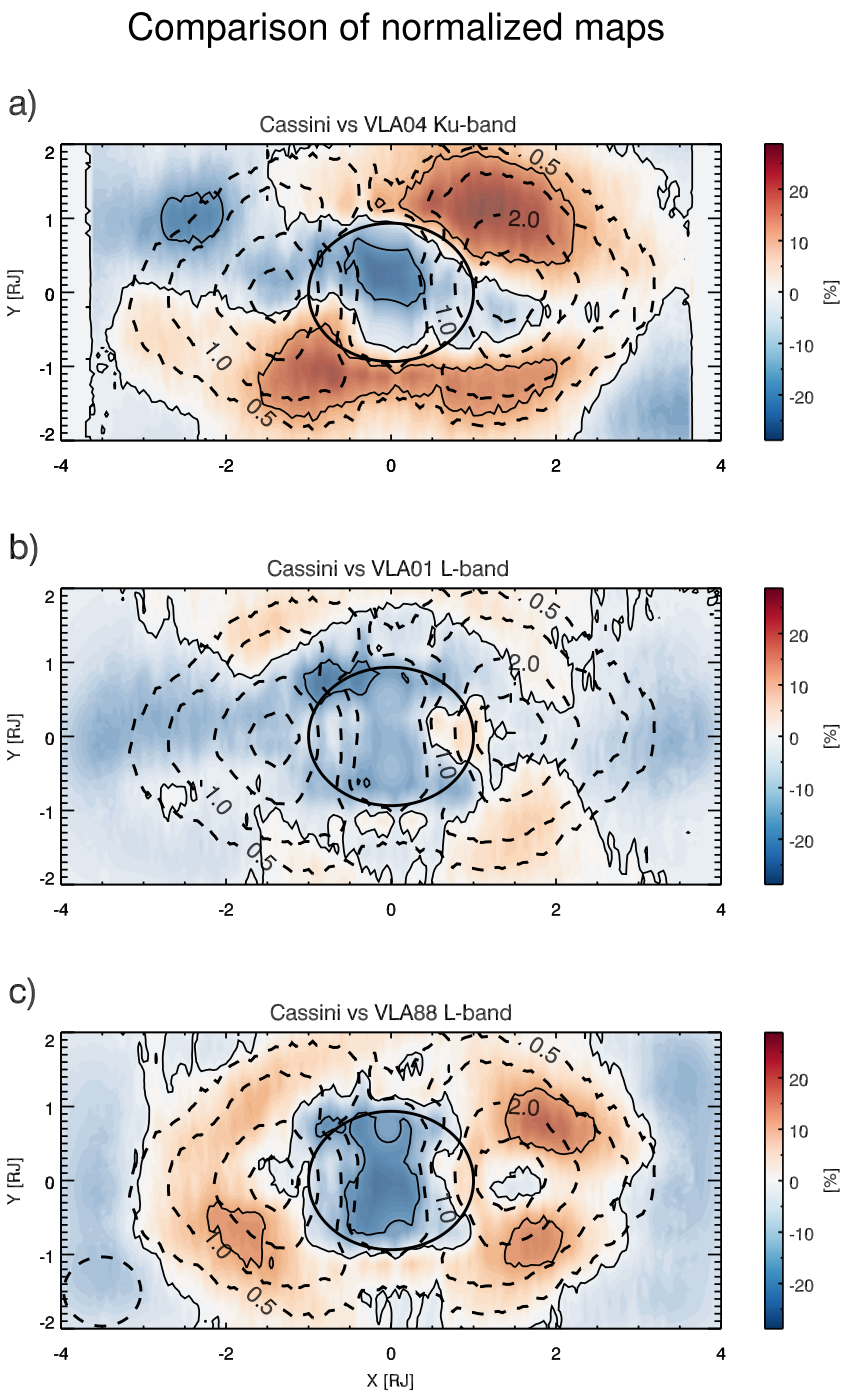

Fig. 6. Normalized differences between VLA maps and the Cassini (13.8 GHz) synchrotron radiation maps. Red shading indicates an enhancement of the Cassini map, blue a depletion of synchrotron electrons. The dashed contours show the Cassini map for spatial comparison. In all maps Jupiter's contribution was removed by subtracting a limb darkened disk. The three panels compare the Cassini map to: (a) the VLA 2004 Ku-band (14.9 GHz) map (Kloosterman et al., 2008); (b) VLA 2001 L-band (1.4 GHz) map (Santos-Costa et al., 2014); and (c) VLA 1988 L-band (1.4 GHz) radio map (Santos-Costa et al., 2014). (For interpretation of the references to color in this figure legend, the reader is referred to the web version of this article.)

recalculated VLA calibrations at 13.8 GHz (de Pater et al., 2016).

Additionally, the limb darkening coefficient was introduced to study the polar residuals, where the temperature as a function of emission angle, θ, is $T \propto \cos(\theta)^p$. These residuals were originally attributed to an insufficient brightness distribution that could not resolve the fine structure of the brightness model. Considering that the east-west limb darkening coefficient is normally given by $p = 0.08$, (de Pater et al., 2016), it is astounding that all scans converge to a weaker limb darkening coefficient of $p = 0.05$. This could be attributed to a strong synchrotron signal from the poles, which has not be observed before. The more likely explanation is a depletion of ammonia at the poles. Interestingly, a similar conclusion had been reached by studying high frequencies maps of Jupiter (de Pater, 1986).

5. Discussion

As discussed above and summarized in Section 5.1, the radiation belts appeared to have undergone significant changes both in total electron content and in the morphology of the radiation maps. While changes in the synchrotron radiation belts have occurred before (Klein

et al., 1989; de Pater et al., 1995; Santos-Costa et al., 2008), such drastic changes warrant a more detailed discussion. In this section we discuss possible scenarios that could explain these changes.

5.1. Summary of the observation

We summarize the main observations that led to our conclusion of Jupiter's disturbed state as follows:

5.1.1. Depletion of energetic electrons

The flux density (Fig. 5) is a proxy for the number density of relativistic electrons in the magnetosphere; the more particles are present, the higher is their combined emitted power. The integrated flux density of 1.10 Jy as derived from the Cassini measurements is suggestive of a low number density of electrons in Jupiter's magnetosphere. This is in contrast to the concurrent measurements at lower frequencies, especially at a frequency of 327 MHz (P-band) (Santos-Costa et al., 2014), which indicates an increase in flux density within the natural variability. The model curve that was fit to the 2001 measurements is based on standard modeling coefficients, but forced a depletion of high-energy particles by truncating the maximum electron energy that was considered in the simulation.

5.1.2. Cassini radio maps

The radio maps present the distribution of the electrons across the radiation belts. Comparison with VLA high-frequency maps identified an electron concentration at high latitudes, with observational evidence that the increase is concentrated around the secondary emission rings. This observation requires a mechanism to re-distribute energetic electrons, and preferentially pitch angle scatter the ultra-relativistic electrons to the secondary emission rings.

5.2. Energy dependent processes

Variations in the synchrotron spectrum are an indication of changes to the energy population, and as such affect the whole spectrum (de Pater and Dunn, 2003). The low flux density at high frequencies in contrast to the slightly enhanced emission at low frequency, however, indicates that processes must be acting preferentially on the energetic fraction of the electrons. Such features have so far not yet been considered in models (de Pater and Dunn, 2003; Santos-Costa et al., 2008).

5.2.1. Flux density

Most processes considered in previous research allow for a hardening of the spectrum, that is an increase of flux density at higher frequencies. This is in contrast to the Cassini measurement that indicates a softening of the spectrum. Fluctuations in the energetic electron number density naturally affect the integrated emitted power where the fluctuations correspond to a lag time in agreement with the inwards diffusion of the particles (Klein et al., 1989; Bolton et al., 1989; de Pater and Goertz, 1994; Galopeau and Gerard, 2001). The inwards diffusing electrons are well mixed so that changes affect the synchrotron radiation across all frequencies and thus cannot explain localized changes such as the observed depletion at high frequencies. Furthermore, previous studies have highlighted a lack of correlation between the solar wind conditions and the synchrotron flux density in the 1996–2002 window (Santos-Costa et al., 2008; 2014).

There is observational evidence that the flux density spectrum is more variable at 3.3 GHz compared to measurements at 1.4 GHz as inferred by changes in the spectral index (Galopeau and Gerard, 2001), however, no explanation is offered for the source of the energy dependence. Nevertheless, the research at 3.3 GHz probes a different electron population than Cassini's measurements, so that the question remains if this variability also pertains to the ultra-relativistic electron population.

Interaction with dust particles in the feeble rings of Jupiter can affect the electron population through pitch angle scattering and energy degradation (de Pater and Goertz, 1990; Santos-Costa et al., 2014). The interaction with dust particles significantly alters low energy electrons through absorption and inelastic scattering. The faster the electron, the less affected they are by the presence of the dust particles so that interaction with dust particles leads to overall hardening of the spectrum (de Pater and Goertz, 1990). This hypothesis was confirmed by Santos-Costa and Bolton (2008). Additional to the impact of dust particles, other factors such as radial transport, the sweeping effects of moons, and effects of rapid gyration were studied. Of all factors considered during the analysis, all factors resulted in a hardening of the spectrum, except when ignoring the moonlet's motion resonance with particles (de Pater, 1981; de Pater et al., 1997a; Santos-Costa and Bolton, 2008).

Singular events such as impacts from large cometary bodies can alter the radiation belts on very short timescales. There is no observational evidence for an impact before the 2001-flyby, which does however not exclude the possibility. The impact of cometary bodies was studied extensively during the Shoemaker-Levy 9 impact (de Pater et al., 1995; Brecht et al., 2001; Harrington et al., 2004 and references therein). The comet caused a system of shockwaves to travel through the magnetosphere in combination with an increased mass loading of the ionosphere. The combined effects resulted in an increase in radial diffusion (de Pater et al., 1995), which in turn energized particles and caused an increase in flux density. The intensification (10% at 0.3 GHz and up to 45% at 5 GHz) was more pronounced at shorter wavelengths leading to a hardening of the spectrum.

A similar conclusion was reached when observing long-term trends after the Shoemaker-levy 9 impact, which found an enhanced variability at higher frequencies and argues for processes that pitch angle scattering effects energetic particles more drastically (Galopeau and Gerard, 2001).

In conclusion, most known processes lead to an enhancement at higher frequencies, and processes that remove particles were not considered so far. There are two remaining explanations left that could explain a depletion at higher energies.

Lack of acceleration. The simplest explanation that could explain the lack of electrons is that the electrons have not been accelerated sufficiently to reach the required energy levels. This hypothesis is consistent with the depletion of ultra-relativistic electrons and also the enhancement at lower frequencies.

The current state of the art models use radial inwards diffusion (Santos-Costa and Bourdarie, 2001; de Pater, 1981) that causes energization of the electrons by conserving the first adiabatic invariant for an increasing magnetic field; where acceleration in this paper indicates an increase in kinetic energy. The diffusion is most likely caused by fluctuations in the ionosphere of Jupiter (Brice and Mcdonough, 1973) and as such present time-variant phenomena in line with the Cassini observations.

There are, however, major concerns that discount this theory. A weakened radial diffusion should also cause an outward motion of the peaks (de Pater and Goertz, 1994), however, the radiation maximum at $\sim$1.45 is in good agreement with other observations (de Pater and Klein, 1989) and does not confirm an outwards movement. Quite the contrary, the radiation peaks at high frequency should be located further outwards, due the shorter lifetime of energetic particles (de Pater, 1991), where the 5 GHz peak locations were $\sim$0.05 R_J further outwards than 1.4 GHz counterparts. In terms of pitch angle diffusion, radial diffusion should cause an increase pitch angle (de Pater et al., 1997a; de Pater and Lissauer, 2001). Considering that we observe an expanded magnetosphere as seen in 2001 (Santos-Costa et al., 2014), it is very unlikely that a lack of acceleration can explain the observations.

Relativistic electron dropout. The counterpart to above explanations is the existence of processes that remove particles from the

magnetosphere, preferentially the energetic particles. To date, no such processes are included in radiation belt models of Jupiter. The terrestrial radiation belts have received considerably more attention and as such are more advanced than their Jovian counterpart. During magnetospheric storms, which compress the dayside magnetosphere substantially, spacecraft have observed Relativistic Electron Dropouts (RED), which describe a sudden depletion of the energetic particles on very short timescales. Despite some fundamental differences between the two magnetospheres, such processes are the best candidate for explaining the 2001 radiation belts.

5.3. Review of relativistic electron dropouts in Earth's magnetosphere

The first in-situ observation of a sudden depletion in MeV electrons in the terrestrial radiation belts come from the Explorer 12 spacecraft's particle detectors (Freeman, 1964), which highlighted the variable dynamics in the magnetosphere. The impact of precipitating electrons was also confirmed by ground-based observations through their effects on the auroral zones (Bailey, 1968). This section aims at summarizing the most important points of relativistic electron dropouts; the interested reader is referred to more specialized literature for an in-depth review (Thorne and Kennel, 1971; Summers et al., 1998; Takahashi, 2006; Thorne et al., 2006; Millan and Thorne, 2007).

Rapid electron dropouts were found to be a common occurrence during magnetospheric storms and substorms, which cause a compression of the magnetosphere on the sunward side, and results in a injection of charged particles in the radiation belts. The events are initiated around the midnight sector, causing a redistribution of electrons through a combination of acceleration and scattering processes (Millan and Thorne, 2007). The acceleration causes a redistribution of the electrons, resulting in drift shell splitting, and the eventual loss to the magnetosheath. Contrary, pitch angle scattering can decrease the pitch angle of particles substantially and cause particles to be lost to the atmosphere. The depletion of energetic particles in the radiation belt, which is very short lived (<1 h) (Selesnick and Blake, 2002), is followed by a period of acceleration, that requires injection of electrons into the magnetosphere and rapid acceleration to replenish the belts. The source of these particles is not yet fully established, but the solar wind is cited as the most probable source (Selesnick and Blake, 2002). The post-storm conditions determine the final state of the radiation belt, and as such both depletion and enhancement were observed with spacecraft (Reeves et al., 2003).

Wave-particle interactions describe the effect of fluctuations pertinent to the plasmasphere on the electrons. There is a wide range of waves present in the magnetosphere of the outer planets (Zarka, 2004). The most important waves include Hiss, Chorus and Electromagnetic Ion Cyclotron (EMIC) waves, where the level of wave activity to this date is inconclusive (Bolton et al., 2004). Modeling and observations of the terrestrial case have provided clues how best to explain the various events that occur during the relativistic electron dropout events (Kennel and Petschek, 1966; Thorne and Kennel, 1971). The effect is enabled when the gyromotion of the electrons resonates with the frequency of the plasma waves (Millan and Thorne, 2007), which leads to conditions for acceleration and pitch angle scattering. As such, the interaction with the plasma waves is dependent on the electrons' properties (such as energy and pitch angle) and the local magnetic field strength (Millan and Thorne, 2007):

$$\omega - k_{\|} v_{\|} = \frac{n\Omega_e}{\gamma} \tag{5}$$

$\boldsymbol{\omega}$ [rad/s] Frequency of the plasma waves
$\boldsymbol{k}_{\|}$ [$-$] Parallel wavenumber of plasma waves
$\boldsymbol{v}_{\|}$ [m/s] Parallel velocity of electrons
$\Omega_{\boldsymbol{e}}$ [Hz] Gyrofrequency of the electrons
$\boldsymbol{n}$ [$-$] Harmonics indicator of resonance
γ [$-$] Lorentz factor

Despite the possibility of oblique propagation, most models assume parallel propagation along the field lines, so that the velocity vector parallel to the field lines is of main interest.

Electromagnetic ion cyclotron waves. EMIC waves, the main candidate for resonance at Jupiter, are caused by temperature anisotropies of the ion population and propagate below the gyrofrequency of ions in the plasma. Protons and heavier ions injected during magnetic storm conditions give rise to the ring currents, which in turn excite the EMIC waves (Jordanova et al., 2001). Whereas hiss and chorus waves are right-handed polarized waves, EMIC waves are left-handed. For resonance conditions, the electrons have to overtake the waves with sufficient velocity to invert the polarization in the electron frame (Millan and Thorne, 2007). As a consequence, only electrons with sufficient velocity can reach the resonance conditions, while lower energy electrons are unaffected. This property makes them the prime candidate for the scattering of relativistic electrons and has been inferred for relativistic electron depletion in the terrestrial radiation belts (Thorne and Kennel, 1971).

The waves can lead to both an energization and rapid pitch angle scattering of ultra-relativistic electrons (Thorne et al., 2006). Whereas diffusion is very inefficient for resonance with ultra-relativistic particles, pitch angle scattering is very effective, scattering electrons within just a few cycles of interactions (Summers et al., 1998). These effects have been simulated and confirmed by recent spacecraft measurements (Jordanova et al., 2008), which were able to confirm both the depletion of electrons and the simultaneous presence of EMIC waves at the right frequencies (Zhang et al., 2016; Tsurutani et al., 2016; Shprits et al., 2016). The main physics and the applicability to the Jovian radiation belts are discussed in the following section, along with a short model to prove their applicability.

The EMIC waves propagate below the gyrofrequency, which depends on the mass and charge of the particles and the local magnetic field strength. The propagation efficiency of the wave is determined by the temperature anisotropy, so that closer to the proton-gyrofrequency, the waves are damped and cannot propagate, also known as the stop band. While at lower frequencies the required energy for interaction increases steeply, reducing the number of particles that can be scattered. In the terrestrial belts, the optimal propagation frequency, normalized to the local proton-gyrofrequency, is between 0.7–0.9 (Summers and Thorne, 2003; Thorne et al., 2006), with typical values at Jupiter around 0.8 (Bagenal et al., 1997). The presence of heavier ion species introduces further stop bands at their respective gyrofrequency but also affects the propagation curve in other bands. For example, the presence of He^+ facilitates the interaction in the vicinity of the proton stop band (Thorne et al., 2006).

In the terrestrial belts, these waves have been studied for decades, but there is observational evidence (Zarka, 2004) and physical models of the radiation belts (e.g., for Jupiter (Nénon et al., 2017)) that confirm that the magnetospheres of the outer planets support a wide range of waves. Hence, this process might be acting in Jupiter's magnetosphere and could potentially explain the Cassini observations. Other waves that were considered, but not included here, were Hiss and Chorus waves (Millan and Thorne, 2007; Summers et al., 2008), however, the resulting effects cannot explain the preferential acceleration of energetic particles. Another notable acceleration mechanism that can act on the equatorial electrons is ultra-relativistic acceleration (Summers and Omura, 2007), through an interaction with whistler-mode waves, whose spatial distribution was observed and mapped with Galileo (Menietti et al., 2016).

5.4. EMIC wave conditions at Jupiter

EMIC waves are generated by three mechanisms (Thorne et al., 2006). The first mechanism requires a large-scale injection of plasma ions into the inner magnetosphere, that in turn will lead to an increase in ring current. Large-scale ion flux can produce an anisotropy in the plasma temperature which in turn gives rise to EMIC waves (Kennel and Petschek, 1966). At Jupiter, large-scale convection of ions is provided by the highly variable plasma sources at Jupiter. On the outer edge of the inner magnetosphere, Io's volcanic activity is the primary source of cold plasma and injects large quantities of plasma into the Io plasma torus (Kupo et al., 1976; Divine and Garrett, 1983; Bagenal, 1994). On the inner edge, the ionosphere injects plasma into the magnetosphere (Yelle and Miller, 2004; Garrett et al., 2015), where the plasma density is dependent on the local atmospheric density. The ionosphere responds to solar extreme ultraviolet flux (EUV) and as such is known to fluctuate by orders of magnitude (Yelle and Miller, 2004). It is, therefore, conceivable that at times of intense EUV flux, the ionosphere injects large quantities of plasma into the magnetosphere, causing temperature anisotropies, which sustain EMIC waves.

The second mechanism is based on the compression of the magnetosphere by the solar wind, however, considering the size of Jupiter's magnetosphere this mechanism does not seem plausible.

Lastly, ultra low-frequency (ULF) waves are known to perturb the ion population (Rasinkangas and Mursula, 1998; Ozeke et al., 2017), and as such can give rise to EMIC waves. ULF wave observations require in-situ observations, and thus there is very little information on the existence of such waves in the inner magnetosphere. The Voyager spacecraft reported on ULF waves in the middle magnetosphere (Khurana and Kivelson, 1989), however, spacecraft charging prohibited observations further inwards. Indirect observations gave some hints on the existence of ULF waves (Arkhypov and Rucker, 2006). It is, therefore, conceivable that ULF wave could also excite EMIC waves.

Recent measurements by the Juno spacecraft have found evidence for wave – particle interaction and indirect evidence of ion-cyclotron waves (Kurth et al., 2018).

Simplified model. Summers and Thorne (2003) developed an analytical expression for resonance conditions for EMIC wave interaction in a multiple species plasma, which can be applied to the Jovian magnetosphere.

The authors introduced a nondimensional factor, α^*, that controls the resonance conditions and is dependent on the local magnetospheric properties:

$$\alpha^* = \frac{\Omega_e^2}{\omega_{pe}^2} \tag{6}$$

with,

$$\Omega_e = \frac{qB}{\gamma m_e c} \tag{7}$$

$$\omega_{pe} = \sqrt{4\pi N_e q^2/m_e} \tag{8}$$

Ω_e [Hz] Gyrofrequency of the electrons
B [T] Local magnetic field strength
ω_{pe} [rad/s] Plasma frequency
N_e [m^{-3}] Plasma density, cold electrons below 10 keV
q [C] $= 1.60 \times 10^{-19}$, Charge of an electron
m_e [kg] $= 9.11 \times 10^{-31}$ Mass of an electron
c [m/s] $= 3.0 \times 10^{8}$ Speed of light

It is clear that both the magnetic field strength, B, and the local cold plasma density play a crucial role in controlling the wave-particle interaction, where a smaller value for α^* is preferable for interaction. In other words, this requires a combination of dense cold plasma in conjunction with a weak magnetic field, the opposite of the inner magnetosphere of Jupiter. At larger α^* values higher energies of the electrons are required for interaction. As explained above, the resonance conditions are influenced by the ion composition, and for a multispecies plasma (denoted by the subscript $_i$) the propagation speed of the EMIC waves (Stix, 1992) is given by:

$$\frac{c^2k^2}{\omega^2} = 1 - \frac{\omega_{pe}^2}{\omega(\omega + |\Omega_E|)} - \sum_{i=1}^{n} \frac{\omega_{pj}^2}{\omega(\omega - \Omega_j)} \tag{9}$$

ω_{pj} [Hz] Ion plasma frequency, for ion species i
Ω_i [Hz] Ion-gyrofrequency of ion species i

This relationship can be normalized by taking the relative abundances of the main species into account:

$$\frac{1}{u^2} = 1 - \frac{1}{\alpha^* \epsilon x}\left(\frac{1}{1+\epsilon x} + \sum_{i=1}^{n} \frac{\eta_i}{m_i/m_p x - 1}\right) \tag{10}$$

u [−] Dimensionless wave phase speed
x [−] Dimensionless wave frequency, normalized by the proton-gyrofrequency
ϵ [−] $m_e/m_p = 0.00054$, electron-proton mass ratio
η_i [−] Fractional abundance of ion species i
m_i [kg] Mass of ion species i

The parameter u controls the propagation speed of EMIC waves through the plasma, which translates into a minimum energy that the electrons require for resonance. The highest velocity is reached when the electrons are moving parallel to field lines, that is at minimum pitch angle. The minimum energy for interaction is then given by Summers and Thorne (2003):

$$E_{\min} = \left(1 - \frac{v_\parallel^2}{c^2}\right)^{-1/2} - 1 \tag{11}$$

Where,

$$\frac{v_\parallel}{c} = \frac{u\left[\epsilon^2 x^2 + (\epsilon^2 x^2 + u^2(1-\epsilon^2 x^2))^{1/2}\right]}{\epsilon^2 x^2 + u^2} \tag{12}$$

E_{min} [MeV] Minimum energy for interaction with EMIC waves of phase speed ω
$v_\parallel$ [m/s] Velocity parallel to the magnetic field lines.

Jovian plasmasphere. The plasma conditions in the inner magnetosphere are best studied through in-situ exploration, something that the Jovian system is lacking. Despite the limited exploration of the inner magnetosphere, we can still perform a feasibility study using the current state of the art of knowledge. The Galileo probe before entering the Jovian atmosphere (Fischer et al., 1996; Mihalov et al., 2000) was able to measure the energetic particle flux of protons, helium, and heavier-than-helium particles.

The magnetic field at Jupiter is based on a simple dipole model that assumes an inclined dipole with a magnetic moment $1.56 \times 10^{20} Am^2$ (Yoder, 1995). Lastly, the most important parameter is the cold plasma (ions below 10 keV) density, which constitutes the bulk of the plasma in the magnetosphere. The cold plasma is produced by a variety of sources:

- Io: Volcanic activity supplies the magnetosphere continuously with ions and neutrals (Kupo et al., 1976; Thomas et al., 2004). As the particles are ionized, they are corotating with the magnetic field, and quickly form a plasma torus around Io's orbit. The electron density varies by more than an order of magnitude depending on the

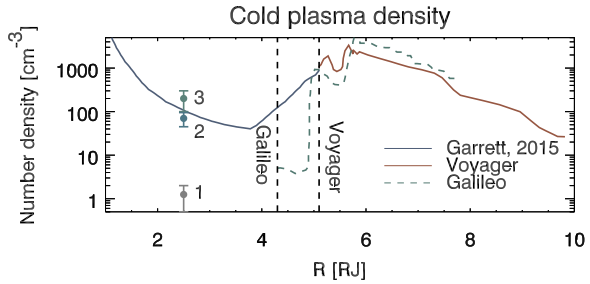

Fig. 7. Cold plasma density overview of models and measurements from different indirect and direct observations. The purple line is based on the Divine and Garrett radiation model (Divine and Garrett, 1983; Garrett et al., 2015), the blue line is based on Voyager measurements (Warwick et al., 1979), the yellow line is based on Galileo measurements (Bagenal et al., 1997). The dots correspond to remote observations: measurement point 1 (Hamilton and Krüger, 2008), measurement point 2 (Wang et al., 1998), measurement point 3 (Arkhypov and Rucker, 2013). The uncertainties are 10% estimates, as no information was provided in the original publications. (For interpretation of the references to color in this figure legend, the reader is referred to the web version of this article.)

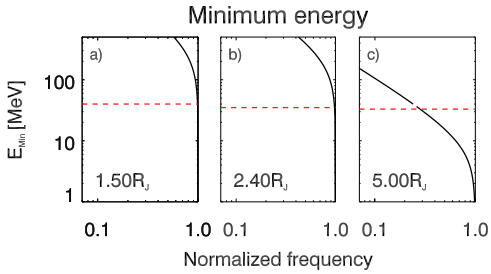

Fig. 8. The minimum energy required for electrons to overtake EMIC waves with sufficient velocity. The red line indicates the particles' energy that Cassini is sensitive to (40, 37, 30 MeV, respectively). Three regions are selected, where (a) refers to the inner magnetosphere where the majority of the signal is created, (b) refers to the region just inside of Amalthea orbit, and (c) refers to the region where the Io plasma torus is truncated. Electrons that are in resonance must have an energy around a normalized frequency ~0.8 and above the black line. (For interpretation of the references to color in this figure legend, the reader is referred to the web version of this article.)

location of the sampling (Gurnett, 2001).

- Ionosphere: Nagy et al. (1986) suggested early on that the ionosphere is a source of cold plasma. Photoionization of neutral particles by EUV flux produces ions in the upper thermosphere, where the number density quickly drops off with increasing altitude (Hinson et al., 1997; 1998). Radio occultation measurements revealed orders of magnitude fluctuation in the ionospheric density (Yelle and Miller, 2004).
- Jovian rings: The rings can contribute to the cold plasma through photoionization, such as observed in Saturnian ring system (Coates et al., 2005). Whereas the rings are known to absorb electrons, the gaps in the Saturnian ring have an order of magnitude enhanced plasma density compared to the ring region (Ip, 2005).
- Moons: Similar to Europa (Mauk et al., 2003; Kollmann et al., 2016) and Io (Thomas et al., 2004), Amalthea might have a plasma torus associated with it. Sputtered surface material can escape the weak gravitational influence and produce a plasma torus around the orbit of Amalthea (Arkhypov and Rucker, 2013). The existence of several small-scale objects in the vicinity of Amalthea supports the hypothesis that the small moonlet is surrounded by a neutral cloud (Fieseler et al., 2004), which in turn would quickly be ionized and form into a plasma ring.

Fig. 7 summarizes the main models and observations for Jupiter's inner magnetosphere cold plasma density. Whereas the synchrotron electron density can be obtained from their radio emissions, the cold plasma is inferred from the local cut-off plasma frequency (see Eq. (8)) and enables an upper bound on the cold plasma density. Voyager 1 (Warwick et al., 1979) and Galileo (Bagenal et al., 1997) were able to retrieve these quantities, depicted by the blue and yellow solid lines in Fig. 7. Both spacecraft sampled the middle magnetosphere (10–40 R_J), enabling a good estimate of the Io plasma torus. The torus can be divided in a warm, dense outer torus (~2000 cm^{-3}) and a colder, less dense inner torus (~1000 cm^{-3}). Despite the expectation that Io's plasma torus is symmetric inwards and outwards (Herbert et al., 2008), both spacecraft measured a sudden drop in cold plasma density inwards from ~5 R_J, where the density drops by two orders of magnitude over a distance of 0.05 R_J (Bagenal et al., 1997). This seems to indicate a truncation of the inner torus. At present, there are no explanations for such a sharp drop in density (Thomas et al., 2004). The low velocity could cause the cold plasma to collapse to the spin equator, and the spacecraft's latitude could sample the depleted region outside of the spin equator. Herbert et al. (2008) proposed a similar explanation that the torus can simply no longer be observed due the lack of power source for the emission. Lastly, the plasma model inwards of Io is based on two in-situ observations, in an environment that is characterized by large fluctuations.

The Galileo probe and the Pioneer spacecraft traversed the inner magnetosphere, but they were only able to measure the high energetic flux and not the cold plasma. Remote sensing of the cold plasma stems from observing the effect of plasma on other radio emissions (Arkhypov and Rucker, 2006; 2013; Wang et al., 1998) or the ring particle distribution (Hamilton and Krüger, 2008). The latest model for the inner magnetosphere plasma density (Garrett et al., 2015) is in most parts based on the original Divine and Garrett model (Divine and Garrett, 1983), with some updates on the Io plasma torus and the ionosphere. The purple curve in Fig. 7 displays the latest iteration of the plasma density inside of Io's orbit based on the latest model (Garrett et al., 2015).

When discussing the cold plasma density, any information from the inner magnetosphere is at best a snapshot of a highly diverse region. Variability in the source naturally propagates to the plasma density, therefore, any measurement attempt must bear in mind the spatio-temporal variations.

Resonance conditions. Based on the above discussion of the plasmasphere, we calculate the minimum energy for resonance conditions as a function of distance from Jupiter. In the vicinity of Io's plasma torus, a dense cold plasma with a weak magnetic field create conditions that are favorable for interaction (Horne et al., 2008). Further inside, the decreasing plasma density increases the minimum energy required for interaction as calculated by Eq. (11). The red line in Fig. 8 indicates the energy that Cassini is sensitive to, based on the approximate relationship for the observing frequency $\nu = 4.8E^2B$ (Carr et al., 1983), where the magnetic field strength is taken at the mirror points. The black line indicates the level of energy that the electrons must have to interact with the EMIC waves, where resonance can occur on the right of the line.

An estimate of the pitch angle diffusion coefficient requires information on the power spectral density of the EMIC waves and the cold plasma density, two quantities that require in-situ observations yet to be made. Qualitatively, the interaction timescales only requires a few gyrations to pitch angle scatter the electrons (Summers and Thorne, 2003), where the gyration period around the location of Amalthea is on order of 10^{-5} s, and the bounce average is on order of seconds (de Pater, 1981). This should be compared to the lifetime against local losses of electron of a few months to a year. (de Pater and Goertz, 1990).

For optimal interaction, the normalized frequency should be around

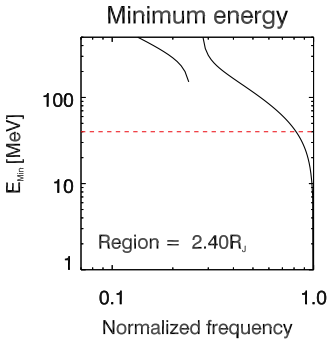

Fig. 9. Resonance conditions for a highly disturbed plasmasphere, by a ten-fold increase in cold plasma density. Energetic electrons (>33 Mev) are in resonance with the EMIC waves and thus could undergo rapid pitch angle scattering. This energy corresponds to the energy that Cassini is sensitive to.

~0.8. The region inside of Amalthea (R_J <2.5) is of highest interest, as electrons at these distances mirror in the secondary emission rings, and thus correspond to the region that experienced enhancement. Fig. 8b, however, indicates that for normal plasma conditions, the energy required for interaction is around 200 MeV, far above the level expected for electrons at Jupiter. Further inwards, the minimum energy is even higher, whereas further out (panel c), the electrons most likely do not have sufficient energy, as seen by the low brightness temperatures in the Cassini maps. Therefore, an undisturbed plasmasphere does not support electron scattering by EMIC waves. This can explain the standard flux density in 1991 (de Pater and Dunn, 2003) and 2004 (Kloosterman et al., 2008). However, we are looking for an extreme event, and thus it is worthwhile to consider the case of a highly disturbed plasmasphere.

Disturbed magnetosphere. As explained above the plasmasphere is supplied by highly variable sources that can fluctuate by orders of magnitude and consequently the enhanced sources can locally change the plasma density. The question remains if an enhancement in the plasma density can explain the observations. The resonant conditions for an order of magnitude increase in the cold plasma density are shown in Fig. 9, where the resonance condition for the normalized frequency intersects the electron population at an energy level of 33 MeV. Particles at higher energies, therefore, are rapidly pitch angle scattered and removed from the magnetosphere.

EMIC wave particle interaction, which is calculated here based on the velocity parallel to the field (see Eq. (11), require other processes to redistribute the electrons and achieve small pitch angles. The radio maps point at the region inwards of Amalthea, as the motion of the moonlet through the plasma excites whistler mode waves (de Pater, 1981; Gurnett, 1995; de Pater et al., 1997a; Menietti et al., 2005), which in combination with the dust interactions (Santos-Costa and Bolton, 2008) can cause enhanced pitch angle scattering of electrons.

5.5. Summary of the process

The observed conditions at Jupiter imply that energetic particles have been removed, while lower energy particles were left unaffected. Whereas such a behavior cannot be explained with current synchrotron radiation models, this behavior has been observed in the terrestrial van Allen belts: the interaction of electromagnetic waves with the gyrating electrons. To be specific, resonance with EMIC waves requires energetic electrons with small pitch angles to overtake the electromagnetic fluctuations and reverse the polarity of the waves to achieve resonance. In the proposed scenario, when electrons diffuse past Amalthea, they undergo pitch angle scattering due to interaction with whistler mode waves. As their pitch angle is decreased, the electrons reach resonance conditions and are rapidly scattered to higher latitudes and into the loss cone. In such an event, we would expect an enhancement at higher latitudes, and an overall depletion of energetic electrons above the threshold resonance energy.

6. Conclusion

The disagreement between the initial retrieval of Jupiter's synchrotron radiation with ground-based observations and simulations (de Pater and Dunn, 2003) prompted a rigorous re-analysis of the raw data and improved our understanding of the variability intrinsic to the Jovian synchrotron radiation.

The calibration algorithm specifically developed for the Cassini Radar system was applied to the Jupiter raw data, incorporating the improved understanding of the radiometer, obtained from a decade of operation at Titan. The updated algorithms included a refined beam pattern, an improved thermal brightness model for Jupiter, and the latest calibration factors with absolute calibration accuracy below the 1% level.

The uncertainties intrinsic to the instrument, as well as the parameters of the brightness model, were obtained by fitting the Cassini observations to the brightness model of Jupiter. The goodness-of-fit is based on five selected regions, using a-priori knowledge on the synchrotron radiation structure. The Markov-Chain Monte-Carlo optimization simultaneously solved for the uncertainties in the beam position, the parameters of the brightness model and the solutions' sensitivity to these variables.

An in-depth analysis of the uncertainties in the instrument revealed that the oscillator drifts about 0.5 s per day, and leading to a misrepresentation of the beam location. Similarly, the uncertainty analysis confirmed that the beam location is shifted from the boresights of the radio antenna, and shows signs of spacecraft jitter below the pointing accuracy of Cassini. The brightness model parameters allowed for constraining the disk-averaged brightness temperature to 158.6 K ± 2.4 K, and a depletion of ammonia towards the poles as indicated by a limb darkening coefficient of 0.05 compared to 0.08 as cited in literature (de Pater et al., 2016).

The integrated flux density, a measure of the total power emitted by the electrons, was revised to 1.10 Jy ± 0.07 Jy, compared to the 0.44 Jy ± 0.15 of the initial retrieval (Bolton et al., 2002). The variations with longitude as given by the beaming curve are in excellent agreement with predictions. Despite the 2.5 factor increase compared to the initial retrieval, the retrieval still indicates a depletion of energetic particles from the Jovian radiation belts, contrary to the enhanced flux emitted by less energetic particles observed at 1.4 GHz.

The radio maps from Jupiter support the hypothesis (Santos-Costa et al., 2014) that the magnetosphere in 2001 was highly disturbed, as seen by the north-south expansion of the belts. Comparison with similar high-frequency maps shows a drastic enhancement at higher latitudes, demonstrating that the energetic particles must have been re-distributed. A similar conclusion is reached when comparing the normalized maps to the lower frequency observations, where an enhancement in radiation at higher latitudes (i.e. a localized brightening in the secondary emission rings), can be found.

The observations are consistent with a depletion of energetic electrons through energy-dependent pitch angle scattering. Energetic particles are preferentially scattered to higher latitudes, causing a redistribution of the electrons, until they are ultimately lost to the atmosphere. Such processes are known to occur on Earth when the energetic particles resonate with waves in the plasmasphere. While a simple model indicates that the interaction is not feasible for a nominal plasmasphere, a ten-fold enhancement in the cold plasma density allows electromagnetic ion cyclotron waves to propagate and inflict rapid pitch angle scattering on the energetic particles. This process could partially explain the short-term variability of Jupiter's synchrotron radiation, especially at higher frequencies.

Future models should consider including the effects of wave-particle

interactions. The inclusion of these processes allows one to study the interaction in detail, and can also help to improve the predictive capabilities of the synchrotron model. Eventually, this advancement in knowledge will be reflected in the design of the next generation of Jupiter probes, reducing the uncertainty associated with shielding from the energetic particles.

New in-situ observations of the plasma conditions in the inner magnetosphere would improve our understanding of these processes. As Juno's orbit slowly precesses, the spacecraft increasingly samples the inner magnetosphere. The onboard plasma instrument can add further measurement points on the cold plasma density, and establish spatio-temporal variations. Should large fluctuations be present in the plasmasphere, more simulations of the interactions are required, including estimates of the timescales involved in depleting and re-populating the magnetosphere.

Acknowledgments

Part of this work was conducted at the Jet Propulsion Laboratory (JPL), California Institute of Technology, under contract with the National Aeronautics and Space Administration (NASA). We gratefully acknowledge those who designed, developed and operate the Cassini/Huygens mission, which is a joint endeavor of NASA, the European Space Agency (ESA), and the Italian Space Agency (ASI) and is managed by JPL/Caltech under a contract with NASA.

This research was in part supported by NASA Planetary Astronomy (PAST) Award NNX14AJ43G to UC Berkeley and the Justus en Lousie van Effen through the Delft University of Technology.

We would like to thank Daniel Santos-Costa for discussions with regards to the VLA maps and providing the reduced synchrotron maps of 1988 and 2001, Henry B. Garrett for discussions with regards to the inner magnetosphere, and Zhimeng Zhang for insightful information about the Cassini RADAR.

Appendix A. Beam offset

From every scan, the ten solutions of MCMC with minimum cost function were chosen to perform an analysis on the spacecraft pointing. The following subsections discuss the three relevant uncertainties for the beam: an offset in x and y of the boresight, that is the direction of the main lobe, and the time drift, dt, of the onboard oscillator. The horizontal polarization has strong emission features next to the planet, allowing the MCMC to converge to a unique solution. The weaker vertical polarization lacks these strong features so that the MCMC had more problems converging to a solution. This is reflected by the size of the error bars in the following section that indicate the 1 σ variation found in the results.

A1. Time-offset

Fig. 10 represents the oscillator drift that was obtained individually for every fit, with a resolution of 0.1 s in the MCMC parametrization. Both polarizations indicate a similar increase over time: 0.3 s in the course of 10 h, consistent with the 0.5 s drift in 24 h as expected from the on-ground post processing by the Cassini Navigation team [personal communication, 2017]. The nature of the drift however varies. Where the first ten scans indicate a gradual increase in time offset, the second set of scans indicates an exponential increase. Since during the scan the distance between Cassini and Jupiter is changing, one might suspect that light time variations influence this parameter. The light time variations were corrected for in SPICE, and would result in a linear increase and decrease, respectively. It is, therefore, unlikely that the presented quantities are a result of the movement of Cassini.

The results also indicate that both scans start off from a base value of 0.1 and eventually reach 0.4. The scans were not performed immediately after each other, as the spacecraft had to be rotated first. It is possible that the onboard oscillator was corrected between the two sets of scans.

The effect of a positive drift in the oscillator causes the Jupiter model to be offset with respect to its real position. The relatively large beam size convolves the limb crossing residuals with the region of peak synchrotron radiation, and thus it directly affects the synchrotron signal strength. Not properly accounting for the time offset can be easily mistaken for stray thermal emission and result in an artificially reduced signal.

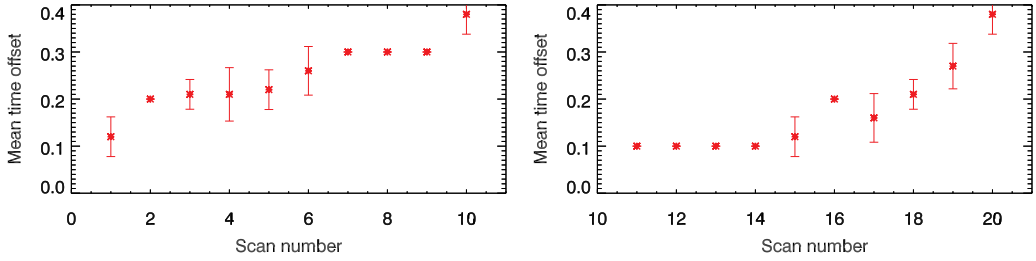

(a) Vertical polarization. (b) Horizontal polarization.

Fig. 10. Oscillator drift.

A2. Beam x-offset

The x-offset is defined in the spacecraft coordinate frame and, therefore, is conserved through the rotation of the spacecraft. When inspecting the outcome in Fig. 11, both sets of scans show to first-degree a constant offset, with a second-degree fluctuation around that mean. This behavior is interpreted as a constant beam offset, due to a misalignment of the main beam, whereas the higher-order variations are the result of spacecraft jitter. Jitter describes the motion of spacecraft below the detection limit of the on-board inertial reference units that establish the pointing of the spacecraft.

The stronger horizontal polarized emissions allows for resolving smaller variations, which explains why there is finer structure in the second set

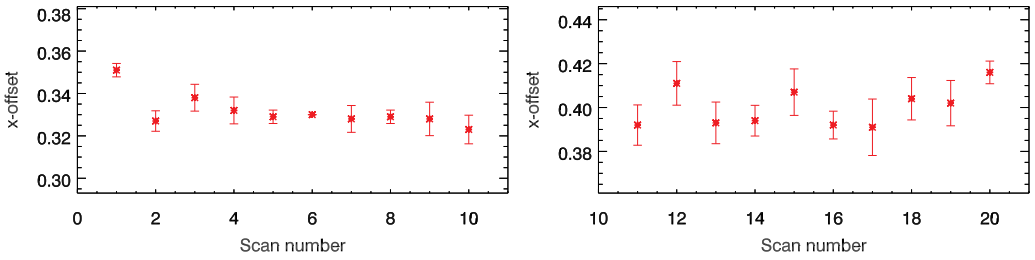

(a) Vertical polarization. (b) Horizontal polarization.

Fig. 11. Beam x-offset.

of scans, compared to the flat behavior of the vertically polarized scans. Nevertheless, the variations are outside of the one sigma variations, indicating that these are indeed statistically significant variations.

Surprisingly, the mean beam-offset differs between the two sets of scans. Since physical changes in the beam offset are very unlikely, this indicates changes in the pointing knowledge of Cassini. These variations are within the pointing requirements, yet are still larger than expected by the pointing analysis (Pilinski and Lee, 2009). This could indicate that the inertial reference unit on-board has a systematic offset.

The effect of misalignment in the x direction is very similar to the time offset, as both uncertainties are acting in the same plane. As a consequence, depending on the beam motion, these uncertainties can be constructive or destructive. Only a very accurate knowledge of the beam shape allows for disentangling these two factors and prevent the uncertainty from propagating into the synchrotron flux.

A3. Beam y-offset

The y-offset also supports the hypothesis that the beam offset is constant, even though the higher order fluctuations seem to be stronger. Due to weak signal coming from the poles it is harder to constrain the y-offset properly, which could partially explain the large variations as seen in Fig. 12. Nevertheless, significant inter-scan variations in combination with small standard deviations from the MCMC are good indications that these variations are real effects as well. Additionally, the single outlier for scan 1 indicates that pointing uncertainties from the spacecraft have propagated into the analysis, as such a large difference cannot be caused by spacecraft jitter alone. The difference in beam offset between the two sets of scans is also present in the y-offset, confirming that a rotation caused a variation in the pointing knowledge. This difference is baffling and requires further investigation.

Disregarding the y-offset causes large residuals at the poles. These residuals at the poles are of special interest, as they probe a little-probed region of Jupiter atmosphere. The initial retrieval used an excessive disk temperature to counter these residuals, which also deflates the synchrotron signal.

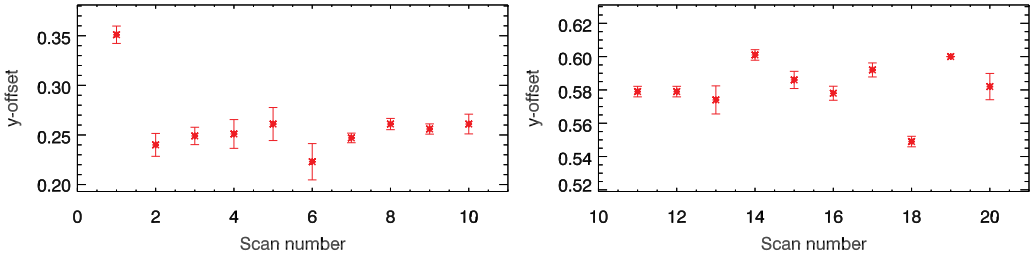

(a) Vertical polarization. (b) Horizontal polarization.

Fig. 12. Beam y-offset.

Appendix B. Synchrotron radiation maps

The individual scans Fig. 13 are shown for the indicated longitude region. The beaming effect can be observed when comparing the peak intensity at different central meridian longitude and variations in the flux density between the East and West peak are due to higher order moments in the magnetic field (de Pater et al., 1997a).

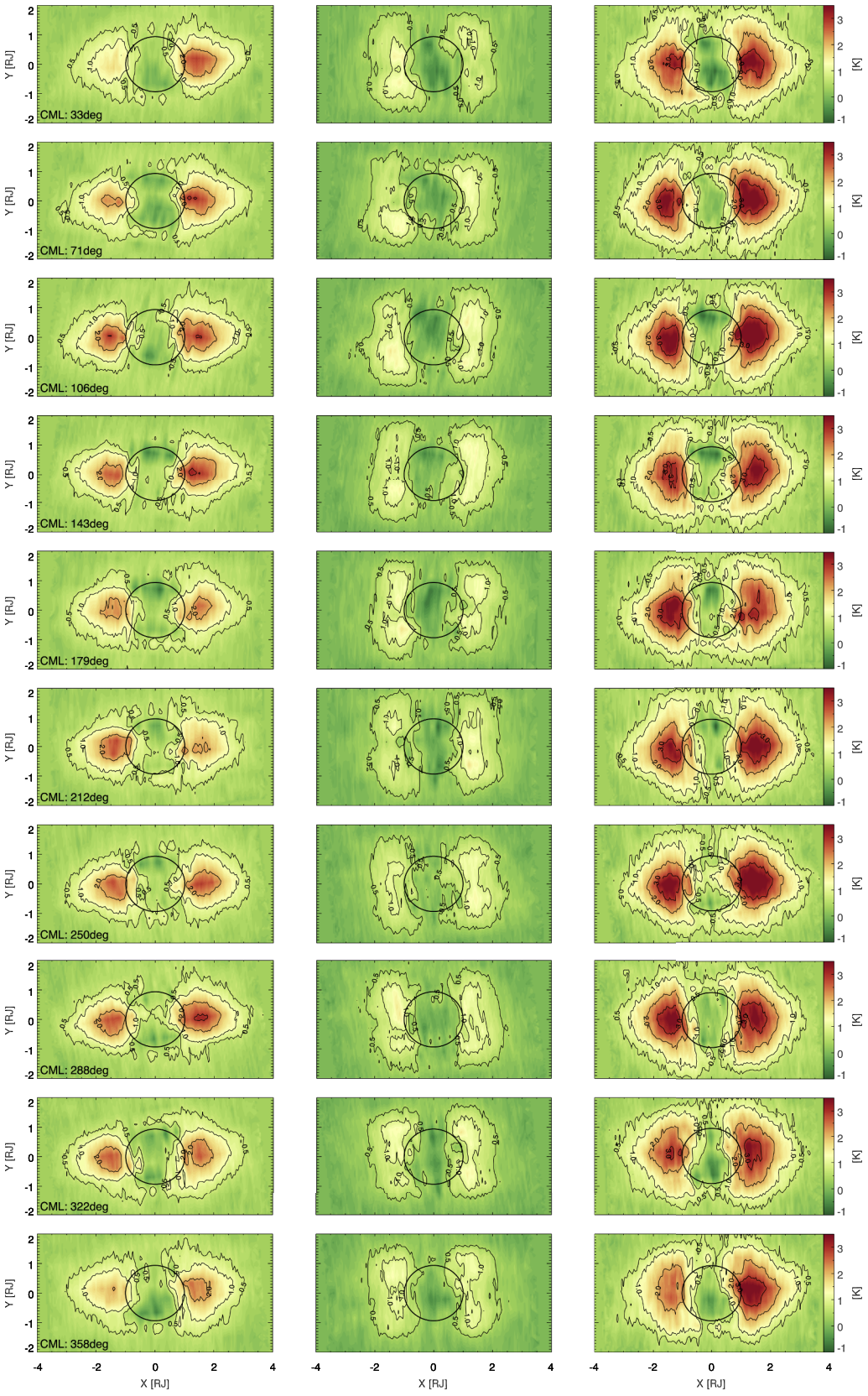

Fig. 13. Individual synchrotron radiation scans rotated to the magnetic equator, with the horizontal polarization in the left column; the vertical polarization in the right column and the combined radiation in the right column. The corresponding CML is given the bottom left corner of the left column. The corresponding combination of uncertainties can be found in Table 6.

Table 6
Uncertainty combination used for generating the individual maps. The first column refers to the oscillator time drift, column two and three are the offset of the beam from boresight in the spacecraft frame, column four is the nadir temperature used for the limb darkened model, and column 6 limb darkening coefficient on the north-south axis.

Scan	*dt* [s]	*dx* [mrad]	dy [mrad]	*T* [K]	*p* [–]
1	0.1	0.35	0.36	161.5	0.05
2	0.1	0.34	0.23	161.25	0.05
3	0.2	0.34	0.23	162	0.05
4	0.2	0.33	0.24	161.75	0.05
5	0.2	0.33	0.25	161.75	0.05
6	0.3	0.33	0.24	161.75	0.05
7	0.3	0.33	0.24	161.5	0.05
8	0.3	0.33	0.26	161.75	0.05
9	0.3	0.33	0.26	161.5	0.05
10	0.4	0.33	0.26	161.5	0.05
11	0.1	0.39	0.57	162.5	0.06
12	0.1	0.41	0.58	162.5	0.05
13	0.1	0.4	0.57	162.5	0.05
14	0.1	0.39	0.59	162.5	0.06
15	0.1	0.4	0.58	162	0.05
16	0.15	0.39	0.57	162.5	0.06
17	0.2	0.4	0.57	162	0.06
18	0.3	0.4	0.55	162	0.05
19	0.3	0.4	0.59	162	0.05
20	0.3	0.41	0.58	161.5	0.05

Supplementary material

Supplementary material associated with this article can be found, in the online version, at doi:10.1016/j.icarus.2018.12.013.

References

Arkhypov, O., Rucker, H., 2006. Ultra low frequencies phenomena in Jovian decametric radio emission. Astron. Astrophys. 452 (1), 347–350.

Arkhypov, O.V., Rucker, H.O., 2013. Decametric modulation lanes as a probe for inner Jovian magnetosphere. Icarus 226 (2), 1214–1224.

Bagenal, F., 1994. Empirical model of the Io plasma torus: Voyager measurements. J. Geophys. Res. Space Phys. 99 (A6), 11043–11062.

Bagenal, F., Crary, F., Stewart, A., Schneider, N., Gurnett, D., Kurth, W., Frank, L., Paterson, W., 1997. Galileo measurements of plasma density in the Io torus. Geophys. Res. Lett. 24 (17), 2119–2122.

Bailey, D., 1968. Some quantitative aspects of electron precipitation in and near the auroral zone. Rev. Geophys. 6 (3), 289–346.

Bolton, S., Gulkis, S., Klein, M., de Pater, I., Thompson, T., 1989. Correlation studies between solar wind parameters and the decimetric radio emission from Jupiter. J. Geophys. Res. Space Phys. 94 (A1), 121–128.

Bolton, S., Janssen, M., Thorne, R., Levin, S., Klein, M., Gulkis, S., Bastian, T., Sault, R., Elachi, C., Hofstadter, M., et al., 2002. Ultra-relativistic electrons in Jupiter's radiation belts. Nature 415 (6875), 987–991.

Bolton, S., Levin, S., Bagenal, F., 2017. Juno's first glimpse of Jupiter's complexity. Geophys. Res. Lett. 44 (15), 7663–7667. https://doi.org/10.1002/2017GL074118.

Bolton, S.J., Thorne, R.M., Bourdarie, S., de Pater, I., Mauk, B., 2004Bolton, Thorne, Bourdarie, de Pater, Mauk. Jupiter's inner radiation belts, Jupiter. The Planet, Satellites and Magnetosphere, Cambridge University Press, Cambridge, UK, 671–688.

Brecht, S.H., de Pater, I., Larson, D.J., Pesses, M.E., 2001. Modification of the Jovian radiation belts by Shoemaker–Levy 9: an explanation of the data. Icarus 151 (1), 25–38.

Brice, N., Mcdonough, T.R., 1973. Jupiter's radiation belts. Icarus 18 (2), 206–219.

Burke, B., Franklin, K., 1955. Observations of a variable radio source associated with the planet Jupiter. J. Geophys. Res. 60 (2), 213–217.

Carr, T., Desch, M., Alexander, J., 1983. Phenomenology of magnetospheric radio emissions. Phys. Jovian Magnetos. 1, 226–284.

Coates, A.J., McAndrews, H.J., Rymer, A.M., Young, D.T., Crary, F.J., Maurice, S., Johnson, R.E., Baragiola, R.A., Tokar, R.L., Sittler, E.C., Lewis, G.R., 2005. Plasma electrons above Saturn's main rings: CAPS observations. Geophys. Res. Lett. 32 (14). https://doi.org/10.1029/2005GL022694.

de Pater, I., 1981. A comparison of the radio data and model calculations of Jupiter's synchrotron radiation, 1. the high energy electron distribution in Jupiter's inner magnetosphere. J. Geophys. Res. Spfundace Phys. 86 (A5), 3397–3422.

de Pater, I., 1991. Radio images of Jupiter's synchrotron radiation at 6, 20, and 90 cm. Astron. J. 102, 795–805.

de Pater, I., Butler, B., Green, D., Strom, R., Millan, R., Klein, M., Bird, M., Funke, O., Neidhöfer, J., Maddalena, R., et al., 2003. Jupiter's radio spectrum from 74 MHz up to 8 GHz. Icarus 163 (2), 434–448.

de Pater, I., Dunn, D.E., 2003. VLA observations of Jupiter's synchrotron radiation at 15 and 22 GHz. Icarus 163 (2), 449–455.

de Pater, I., Goertz, C.K., 1990. Radial diffusion models of energetic electrons and Jupiter's synchrotron radiation: 1. Steady state solution. J. Geophys. Res. Space Phys. 95 (A1), 39–50.

de Pater, I., Goertz, C.K., 1994. Radial diffusion models of energetic electrons and Jupiter's synchrotron radiation: 2. time variability. J. Geophys. Res. Space Phys. 99 (A2), 2271–2287.

de Pater, I., Heiles, C., Wong, M., Maddalena, R., et al., 1995. Outburst of Jupiter's synchrotron radiation after the impact of comet Shoemaker-Levy 9. Science 268 (5219), 1879.

de Pater, I., Jaffe, W., 1984. Very large array observations of Jupiter's nonthermal radiation. Astrophys. J. Suppl. Ser. 54, 405–419.

de Pater, I., Kenderdine, S., Dickel, J.R., 1982. Comparison of the thermal and nonthermal radiation characteristics of Jupiter at 6, 11, and 21 cm with model calculations. Icarus 51 (1), 25–38.

de Pater, I., Klein, M.J., 1989. Time variability in Jupiter's synchrotron radiation. NASA Spec. Publ. 494, 139–150.

de Pater, I., Lissauer, J.J., 2001. Planetary Sciences. Cambridge University Press.

de Pater, I., Sault, R., 1998. An intercomparison of three-dimensional reconstruction techniques using data and models of Jupiter's synchrotron radiation. J. Geophys. Res. Planets 103 (E9), 19973–19984.

de Pater, I., Schulz, M., Brecht, S.H., 1997a. Synchrotron evidence for Amalthea's influence on Jupiter's electron radiation belt. J. Geophys. Res. Space Phys. 102 (A10), 22043–22064.

de Pater, I., van der Tak, F., Strom, R.G., Brecht, S.H., 1997b. The evolution of Jupiter's radiation belts after the impact of Comet D/Shoemaker–Levy 9. Icarus 129 (1), 21–47.

Divine, N., Garrett, H., 1983. Charged particle distributions in Jupiter's magnetosphere. J. Geophys. Res. 88 (A9), 6889–6903.

Dulk, G., Leblanc, Y., Sault, R., Bolton, S., 1999. Jupiter's magnetic field as revealed by the synchrotron radiation belts. II. Change of the 2-D brightness distribution with D_E. Astron. Astrophys. 347, 1039–1045.

Dulk, G., Leblanc, Y., Sault, R., Ladreiter, H., Connerney, J., 1997. The radiation belts of Jupiter at 13 and 22cm. ii. the asymmetries and the magnetic field. Astron. Astrophys. 319, 282–289.

Elachi, C., Allison, M., Borgarelli, L., Encrenaz, P., Im, E., Janssen, M., Johnson, W., Kirk, R., Lorenz, R., Lunine, J., et al., 2004. RADAR: the Cassini Titan radar mapper. Space Sci. Rev. 115 (1–4), 71–110.

Fieseler, P.D., Adams, O.W., Vandermey, N., Theilig, E., Schimmels, K.A., Lewis, G.D., Ardalan, S.M., Alexander, C.J., 2004. The Galileo star scanner observations at Amalthea. Icarus 169 (2), 390–401.

Fischer, H., Pehlke, E., Wibberenz, G., Lanzerotti, L., Mihalov, J., 1996. High-energy charged particles in the innermost Jovian magnetosphere. Science 272 (5263), 856.

Freeman, J.W., 1964. The morphology of the electron distribution in the outer radiation zone and near the magnetospheric boundary as observed by Explorer 12. J. Geophys. Res. 69 (9), 1691–1723.

Galopeau, P., Gerard, E., 2001. Variations of Jupiter's synchrotron radiation: a link with solar activity? Planet. Space Sci. 49 (13), 1379–1391.
Garrett, H.B., Kim, W., Belland, B., Evans, R., 2015Garrett, Kim, Belland, Evans. Jovian Plasma Modeling for Mission Design. Technical Report.
Gibson, J., Welch, W.J., De Pater, I., 2005. Accurate Jovian radio flux density measurements show ammonia to be subsaturated in the upper troposphere. Icarus 173 (2), 439–446.
Ginzburg, V., Syrovatskii, S., 1965. Cosmic magnetobremsstrahlung (synchrotron radiation). Annu. Rev. Astron. Astrophys. 3 (1), 297–350.
Girard, J., Zarka, P., Tasse, C., Hess, S., de Pater, I., Santos-Costa, D., Nenon, Q., Sicard, A., Bourdarie, S., Anderson, J., et al., 2016. Imaging Jupiter's radiation belts down to 127 MHz with LOFAR. Astron. Astrophys. 587, A3.
Gurnett, D., 2001. Electron densities near Io from Galileo plasma wave observations. J. Geophys. Res. A. Space Phys. 106, 26.
Gurnett, D.A., 1995. The whistler-mode bow wave of an asteroid. J. Geophys. Res. Space Phys. 100 (A11), 21623–21629.
Hamilton, D.P., Krüger, H., 2008. The sculpting of Jupiter's gossamer rings by its shadow. Nature 453 (7191), 72–75.
Harrington, J., de Pater, I., Brecht, S.H., Deming, D., Meadows, V., Zahnle, K., Nicholson, P.D., 2004. Lessons from Shoemaker-Levy 9 about Jupiter and planetary impacts. In: Bagenal, F., Dowling, T., Dowling, W. (Eds.), Jupiter: The Planet, Satellites and Magnetosphere. Cambridge Univ. Press, pp. 158–184.
Herbert, F., Schneider, N.M., Dessler, A.J., 2008. New description of Io's cold plasma torus. J. Geophys. Res. Space Phys. 113 (A1). https://doi.org/10.1029/2007JA012555.
Hinson, D., Flasar, F., Kliore, A., Schinder, P., Twicken, J., Herrera, R., 1997. Jupiter's ionosphere: Results from the first Galileo radio occultation experiment. Geophys. Res. Lett. 24 (17), 2107–2110.
Hinson, D.P., Twicken, J.D., Karayel, E., 1998. Jupiter's ionosphere: New results from Voyager 2 radio occultation measurements. J. Geophys. Res. Space Phys. 103 (A5), 9505–9520.
Hirschman, I.I., Widder, D.V., 2012. The Convolution Transform. Courier Corporation.
Horne, R.B., Thorne, R.M., Glauert, S.A., Menietti, J.D., Shprits, Y.Y., Gurnett, D.A., 2008. Gyro-resonant electron acceleration at Jupiter. Nat. Phys. 4 (4), 301–304.
Ip, W., 2005. An update on the ring exosphere and plasma disc of Saturn. Geophys. Res. Lett. 32 (13). https://doi.org/10.1029/2004GL022217. (2005).
Janssen, M., Bolton, S., Levin, S., Sault, R., Klein, M., Gulkis, S., Hofstadter, M., Elachi, C., Johnson, W., Bunker, A., et al., 2001Janssen, Bolton, Levin, Sault, Klein, Gulkis, Hofstadter, Elachi, Johnson, Bunker, et al.. Cassini RADAR/radiometer and VLA observations of Jupiter's synchrotron emission. Plane. Radio Emissions V 229–236.
Janssen, M., Ingersoll, A., Allison, M., Gulkis, S., Laraia, A., Baines, K., Edgington, S., Anderson, Y., Kelleher, K., Oyafuso, F., 2013. Saturn's thermal emission at 2.2-cm wavelength as imaged by the Cassini RADAR radiometer. Icarus 226 (1), 522–535.
Janssen, M., Lorenz, R., West, R., Paganelli, F., Lopes, R., Kirk, R., Elachi, C., Wall, S., Johnson, W., Anderson, Y., et al., 2009. Titan's surface at 2.2-cm wavelength imaged by the Cassini RADAR radiometer: calibration and first results. Icarus 200 (1), 222–239.
Janssen, M.A., Le Gall, A., Lopes, R.M., Lorenz, R.D., Malaska, M.J., Hayes, A.G., Neish, C., Solomonidou, A., Mitchell, K., Radebaugh, J., et al., 2016. Titan's surface at 2.18-cm wavelength imaged by the Cassini RADAR radiometer: results and interpretations through the first ten years of observation. Icarus 270, 443–459.
Jordanova, V., Albert, J., Miyoshi, Y., 2008. Relativistic electron precipitation by EMIC waves from self-consistent global simulations. J. Geophys. Res. Space Phys. 113 (A3) A00A10.
Jordanova, V., Farrugia, C., Thorne, R., Khazanov, G., Reeves, G., Thomsen, M., 2001. Modeling ring current proton precipitation by electromagnetic ion cyclotron waves during the May 14–16, 1997, storm. J. Geophys. Res. Space Phys. 106 (A1), 7–22.
Kennel, C.F., Petschek, H., 1966. Limit on stably trapped particle fluxes. J. Geophys. Res. 71 (1), 1–28.
Khurana, K.K., Kivelson, M.G., 1989. Ultralow frequency MHD waves in Jupiter's middle magnetosphere. J. Geophys. Res. Space Phys. 94 (A5), 5241–5254.
Kita, H., Misawa, H., Bhardwaj, A., Tsuchiya, F., Sakanoi, T., Kasaba, Y., Tao, C., Miyoshi, Y., Morioka, A., 2015. Relation between the short-term variation of the Jovian radiation belt and thermosphere derived from radio and infrared observations. J. Geophys. Res. Space Phys. 120 (8), 6614–6623.
Kita, H., Misawa, H., Tsuchiya, F., Tao, C., Morioka, A., 2013. Effect of solar UV/EUV heating on the intensity and spatial distribution of Jupiter's synchrotron radiation. J. Geophys. Res. Space Phys. 118 (10), 6106–6115.
Klein, M., Thompson, T., Bolton, S., 1989. Systematic observations and correlation studies of variations in the synchrotron radio emission from Jupiter. NASA Spec. Publ. 494, 151–155.
Klein, M.J., 1976. The variability of the total flux density and polarization of Jupiter's decimetric radio emission. J. Geophys. Res. 81 (19), 3380–3382.
Kloosterman, J.L., Butler, B., de Pater, I., 2008. VLA observations of synchrotron radiation at 15 GHz. Icarus 193 (2), 644–648.
Kloosterman, J.L., Dunn, D.E., de Pater, I., 2005. Jupiter's synchrotron radiation mapped with the Very Large Array from 1981 to 1998. Astrophys. J. Suppl. Ser. 161 (2), 520.
Kollmann, P., Paranicas, C., Clark, G., Roussos, E., Lagg, A., Krupp, N., 2016. The vertical thickness of Jupiter's Europa gas torus from charged particle measurements. Geophys. Re.s Lett. 43 (18), 9425–9433.
Kupo, I., Mekler, Y., Eviatar, A., 1976. Detection of ionized sulfur in the Jovian magnetosphere. Astrophys. J. 205, L51–L53.
Kurth, W., Mauk, B., Elliott, S., Gurnett, D., Hospodarsky, G., Santolik, O., Connerney, J., Valek, P., Allegrini, F., Gladstone, G., et al., 2018. Whistler mode waves associated with broadband auroral electron precipitation at Jupiter. Geophys. Res. Lett. 45 (18), 9372–9379.
Li, C., Ingersoll, A., Janssen, M., Levin, S., Bolton, S., Adumitroaie, V., Allison, M., Arballo, J., Bellotti, A., Brown, S., Ewald, S., Jewell, L., Misra, S., Orton, G., Oyafuso, F., Steffes, P., Williamson, R., 2017. The distribution of ammonia on Jupiter from a preliminary inversion of Juno microwave radiometer data. Geophys. Res. Lett. 44 (11), 5317–5325. https://doi.org/10.1002/2017GL073159.
Mauk, B., Mitchell, D., Krimigis, S., Roelof, E., Paranicas, C., 2003. Energetic neutral atoms from a trans-Europa gas torus at Jupiter. Nature 421 (6926), 920–922.
Menietti, J., Groene, J., Averkamp, T., Horne, R., Woodfield, E., Shprits, Y., Soria-Santacruz Pich, M., Gurnett, D., 2016. Survey of whistler mode chorus intensity at Jupiter. J. Geophys. Res. Space Phys. 121 (10), 9758–9770.
Menietti, J.D., Gurnett, D.A., Groene, J.B., 2005. Radio emission observed by Galileo in the inner Jovian magnetosphere during orbit A-34. Planet. Space Sci. 53 (12), 1234–1242.
Mihalov, J., Fischer, H., Pehlke, E., Lanzerotti, L., 2000. Energetic trapped electron measurements from the Galileo Jupiter probe. Geophys. Res. Lett. 27 (16), 2445–2448.
Millan, R., Thorne, R., 2007. Review of radiation belt relativistic electron losses. J. Atmos. Sol. Terr. Phys. 69 (3), 362–377.
Miyoshi, Y., Misawa, H., Morioka, A., Kondo, T., Koyama, Y., Nakajima, J., 1999. Observation of short-term variation of Jupiter's synchrotron radiation. Geophys. Res. Lett. 26 (1), 9–12.
Nagy, A., Barakat, A., Schunk, R., 1986. Is Jupiter's ionosphere a significant plasma source for its magnetosphere? J. Geophys. Res. Space Phys. 91 (A1), 351–354.
Nénon, Q., Sicard, A., Bourdarie, S., 2017. A new physical model of the electron radiation belts of Jupiter inside Europa's orbit. J. Geophys. Res. Space Phys. 122 (5), 5148–5167.
Ozeke, L.G., Mann, I.R., Murphy, K.R., Sibeck, D.G., Baker, D.N., 2017. Ultra-relativistic radiation belt extinction and ULF wave radial diffusion: Modeling the September 2014 extended dropout event. Geophys. Res. Lett. 44 (6), 2624–2633. https://doi.org/10.1002/2017GL072811.
de Pater, I., 1986. Jupiter's zone-belt structure at radio wavelengths: II. Comparison of observations with model atmosphere calculations. Icarus 68 (2), 344–365.
de Pater, I., Sault, R., Butler, B., DeBoer, D., Wong, M.H., 2016. Peering through Jupiter's clouds with radio spectral imaging. Science 352 (6290), 1198–1201.
Pilinski, E.B., Lee, A.Y., 2009. Pointing-stability performance of the Cassini spacecraft. J. Spacecr. Rockets 46 (5), 1007–1015.
Rasinkangas, R., Mursula, K., 1998. Modulation of magnetospheric EMIC waves by Pc 3 pulsations of upstream origin. Geophys. Res. Lett. 25 (6), 869–872.
Reeves, G.D., McAdams, K.L., Friedel, R.H.W., O'Brien, T.P., 2003. Acceleration and loss of relativistic electrons during geomagnetic storms. Geophys. Res. Lett. 30 (10). doi:10.1029/2002GL016513.
Santos-Costa, D., Adumitroaie, V., Ingersoll, A., Gulkis, S., Janssen, M.A., Levin, S.M., Oyafuso, F., Brown, S., Williamson, R., Bolton, S.J., Connerney, J.E.P., 2017. First look at Jupiter's synchrotron emission from Juno's perspective. Geophys. Res. Lett. 44 (17), 8676–8684. https://doi.org/10.1002/2017GL072836.
Santos-Costa, D., Bolton, S., Thorne, R., Miyoshi, Y., Levin, S., 2008. Investigating the origins of the Jovian decimetric emission's variability. J. Geophys. Res. Space Phys. 113 (A1) A01204.
Santos-Costa, D., Bolton, S.J., 2008. Discussing the processes constraining the Jovian synchrotron radio emission's features. Planet. Space Sci. 56 (3), 326–345.
Santos-Costa, D., Bourdarie, S., 2001. Modeling the inner Jovian electron radiation belt including non-equatorial particles. Planet. Space Sci. 49 (3), 303–312.
Santos-Costa, D., de Pater, I., Sault, R., Janssen, M., Levin, S., Bolton, S., 2014. Multifrequency analysis of the Jovian electron-belt radiation during the Cassini flyby of Jupiter. Astron. Astrophys. 568, A61.
Selesnick, R.S., Blake, J.B., 2002. Relativistic electron drift shell splitting. J. Geophys. Res. Space Phys. 107 (A9). SMP 27-1–SMP 27-10. doi:10.1029/2001JA009179.
Shprits, Y.Y., Drozdov, A.Y., Spasojevic, M., Kellerman, A.C., Usanova, M.E., Engebretson, M.J., Agapitov, O.V., Zhelavskaya, I.S., Raita, T.J., Spence, H.E., et al., 2016. Wave-induced loss of ultra-relativistic electrons in the Van Allen radiation belts. Nat. Commun. 7, 12883.
Stix, T.H., 1992. Waves in Plasmas. Springer Science & Business Media.
Summers, D., Ni, B., Meredith, N.P., Horne, R.B., Thorne, R.M., Moldwin, M.B., Anderson, R.R., 2008. Electron scattering by whistler-mode ELF hiss in plasmaspheric plumes. J. Geophys. Res. Space Phys. 113 (A4) A04219.
Summers, D., Omura, Y., 2007. Ultra-relativistic acceleration of electrons in planetary magnetospheres. Geophys. Res. Lett. 34 (L24205). https://doi.org/10.1029/2007GL032226.
Summers, D., Thorne, R.M., 2003. Relativistic electron pitch-angle scattering by electromagnetic ion cyclotron waves during geomagnetic storms. J. Geophys. Res. Space Phys. 108 (A4). https://doi.org/10.1029/2002JA009489.
Summers, D., Thorne, R.M., Xiao, F., 1998. Relativistic theory of wave-particle resonant diffusion with application to electron acceleration in the magnetosphere. J. Geophys. Res. Space Phys. 103 (A9), 20487–20500.
Takahashi, K., 2006. Magnetospheric ULF Waves: Synthesis and New Directions. 169 American Geophysical Union.
Thomas, N., Bagenal, F., Hill, T., Wilson, J., 2004. The Io neutral clouds and plasma torus, Jupiter. The planet, satellites and magnetosphere. 1. Cambridge University Press, pp. 561–591.
Thorne, R.M., Horne, R.B., Jordanova, V.K., Bortnik, J., Glauert, S., 2006. Interaction of EMIC waves with thermal plasma and radiation belt particles. Magnetospheric ULF Waves: Synthesis and New Directions. American Geophysical Union (AGU), pp. 213–223.
Thorne, R.M., Kennel, C.F., 1971. Relativistic electron precipitation during magnetic storm main phase. J. Geophys. Res. 76 (19), 4446–4453. https://doi.org/10.1029/JA076i019p04446.

Tsurutani, B.T., Hajra, R., Tanimori, T., Takada, A., Remya, B., Mannucci, A.J., Lakhina, G.S., Kozyra, J.U., Shiokawa, K., Lee, L.C., Echer, E., Reddy, R.V., Gonzalez, W.D., 2016. Heliospheric plasma sheet (HPS) impingement onto the magnetosphere as a cause of relativistic electron dropouts (REDs) via coherent EMIC wave scattering with possible consequences for climate change mechanisms. J. Geophys. Res. Space Phys. 121 (10), 10130–10156. https://doi.org/10.1002/2016JA022499.

Wang, K., Thorne, R., Horne, R., Kurth, W., 1998. Cold torus whistlers: an indirect probe of the inner Jovian plasmasphere. J. Geophys. Res. 103 (A7), 14987–14994.

Warwick, J.W., Pearce, J.B., Riddle, A.C., Alexander, J.K., Desch, M.D., Kaiser, M.L., Thieman, J.R., Carr, T.D., Gulkis, S., Booischot, A., Harvey, C.C., Pedersen, B.M., 1979. Voyager 1 planetary radio astronomy observations near Jupiter. Science 204 (4396), 995–998. https://doi.org/10.1126/science.204.4396.995.

Yelle, R., Miller, S., 2004. Jupiter's Thermosphere and Ionosphere. 185 Cambridge University Press.

Yoder, C.F., 1995. Astrometric and Geodetic Properties of Earth and the Solar System. Wiley Online Library.

Zarka, P., 2004. Radio and plasma waves at the outer planets. Adv. Space Res. 33 (11), 2045–2060.

Zhang, X.-J., Li, W., Thorne, R., Angelopoulos, V., Ma, Q., Li, J., Bortnik, J., Nishimura, Y., Chen, L., Baker, D., et al., 2016. Physical mechanism causing rapid changes in ultrarelativistic electron pitch angle distributions right after a shock arrival: Evaluation of an electron dropout event. J. Geophys. Res. Space Phys. 121 (9), 8300–8316.

Zhang, Z., Hayes, A., Janssen, M., Nicholson, P., Cuzzi, J., de Pater, I., Dunn, D., Estrada, P., Hedman, M., 2017. Cassini microwave observations provide clues to the origin of Saturn's C ring. Icarus 281, 297–321.